# Measurements of pressure during the forced water entry of a cone into pure and aerated water

Mehdi Elhimer, Aboulghit El Malki Alaoui, Céline Gabillet, Nicolas Jacques

Version of Record: https://www.sciencedirect.com/science/article/pii/S0889974622000603
Manuscript_8d2f72b51ad613dfa424e5a0dbfce942

# Experimental investigation of the pressure distribution during impact on pure and aerated water

Mehdi ELHIMER[1], Aboulghit EL MALKI ALAOUI[1*], Céline GABILLET[2], Nicolas JACQUES[1]

[1] ENSTA Bretagne, UMR CNRS 6027, IRDL, 29806 Brest CEDEX 09, France

[2] IRENav, EA3634-French Naval Academy, 29240 Brest Cedex 9, France

[*] Corresponding author: aboulghit.el_malki_alaoui@ensta-bretagne.com

## Abstract

The phenomena of slamming and wave impacts is ubiquitous in the fields of coastal and naval engineering. The present experimental study examines the pressure distribution arising during the impact of a rigid cone on the free surface of pure water and aerated water initially at rest. The focus is given on the influence of the cone impact velocity and the water aeration on the pressure acting on the cone surface. Three values of the impact velocity $V_i = 5, 7$ and $9$ m/s and three values of the mean air fraction $\alpha_0 = 0\%, 0.35$ % and $1.10\%$ are considered in the impact tests. The instantaneous impact pressure was measured at four different locations on the cone surface. The instantaneous pressure, pressure impulse, as well as pressure maxima and wetted surface expansion velocity, are analyzed. We used a simple model derived from Wagner theory for pressure, pressure impulse, and expansion velocity predictions. In the case of pure water ($\alpha_0$= 0), the results are in good agreement with the predictions by the simple model. Particularly, the scaling of the expansion velocity and the pressure impulse with the impact velocity are shown to be well predicted by the model. The results in the case of aerated water ($\alpha_0$= 0.35% and 1.10%) suggest a decrease of the instantaneous and maximum pressure due to aeration. Self-similarity of the pressure distribution is discussed in case of the aerated flow.

## 1 Introduction

Slamming, the general problem of the impact between a solid surface and liquid surface is ubiquitous in the fields of marine and ocean engineering. This impact event can be extremely

violent, in the particular case where the relative angle between the two surfaces is small. This phenomenon is characterized by a large expansion velocity of the contact surface and a rapid increase of the local loads (pressure) on the structure during the impact. Marine structures such as boat hulls and breakwaters are subjected to repeated and often violent wave impacts. It is well known that these impacts induce large transient loads, which may cause irreversible damages [1]. Therefore, marine structures should be strong enough to withstand the impact loads.

The concept of elementary loading process ELPs was introduced to classify slamming occurrences[2]. It is assumed that each slamming event can be described as a combination of these elementary processes [2,3], either happening simultaneously or in sequence. They are the direct impact (ELP1), the building jet along with the structure (ELP2), and the compression of entrapped gas (ELP3). The first of those three EPLs is the direct impact process which is characterized by the rapid, nearly discontinuous acceleration or deceleration of the flow. This creates pressure waves propagating at the speed of sound in the liquid. Jet impact on a solid wall and flat plat impact on still water surface can be classified into this category.

The second EPL is the most common in engineering applications since it relates to both water entry and breaking wave impacts. It is characterized by the run-up of the liquid along the solid surface, which leads to a large pressure increase on the contact surface. On the contrary, to the EPL1 the contact surface increases continuously with finite speed. EPL2 is the most studied slamming phenomenon, and the most reproducible one in experiments and simulations[2]. First theoretical results were obtained by von Karman[4] for a wedge water entry. Here the contact surface (wetted surface) increases rapidly in comparison to the wedge velocity, and large pressure arises at its surface as a result. In von Karman theory, the elevation of the free surface during the impact is not considered. Wagner [5] introduced a theory also based on potential flow assumption, considering the rise of the free surface, limited to 2D flow. Several enhancements of this theory have been added by subsequent authors to improve the prediction of the pressure distribution [6,7]. For wave impact, the flip-through phenomena occurring during wave impacts on walls, can be also described as an EPL2 and was modeled using pressure-impulse theory[8]. In this case, the water level at the wall accelerates rapidly. As for the water entry, the rapid increase of the wetted surface leads to high pressure values on the wall (solid surface).

Flip through experimental studies are relatively challenging, because of the complexity of the flow taking place in the waves. The impact pressure is also very sensitive to the wave shape before the impact, making these tests poorly repeatable [9]. Engineers use tests on reduced models of ships or breakwaters in wave flume tanks, and the pressure is recorded at several

locations of the structure. The pressure results are generally scaled up using Froude number similarity [10] .

The water entry experiments are comparatively simpler and more repeatable. Comparisons of the Wagner theory predictions with experimental results have been performed in several studies [11–14]. The predictions of the impact force were shown to match experiments on simple shapes for a small deadrise angles. However, the time evolution of the impact pressure and the expansion velocity is not as well documented.

Finally, the third process EPL3 occurs in the case of the entrapment of large air bubbles during the impact, and is less common than EPL1 and EPL2. This entrapment occurs in wave impacts when the crest of the wave hits the wall. The resulting gas pocket is then compressed due to the motion of the wave front towards the wall (combined with the run-up if any). The pocket might oscillate, leading to pressure oscillations with an amplitude and frequency that depends on the pocket size. In the case of water entry, the entrapment may occur if the dead-rise angle is lower than 5°.

A large number of small bubbles might be entrapped in the fluid during the impact, instead of a large gas pocket as in EPL3. Indeed, Hydrodynamic impacts may occur in aerated flows. Aeration is of practical importance in coastal engineering since a large amount of air is entrapped as small bubbles in breaking waves before the impact. It is well-known that the presence of air bubbles in water affects the impact loads [15–20]. The compressibility of an aerated fluid is much higher than that of pure water, as the sonic speed in a diphasic mixture decreases rapidly with the gas volume fraction or void fraction. For instance, in the case of fresh water under atmospheric pressure, it can be shown that the presence of even two percent by volume of air bubbles causes a dramatic reduction of the speed of sound from about 1500 m/s to less than 100 m/s [21].

For example, during violent wave impact on a breakwater, Bullock et al.[22] reported values of the void fraction between 5% and 10% in the vicinity of the wall. Aeration of the flow around a moving structure in water is expected to modify the hydrodynamic loads applied to the structure and the resulting dynamic structural response. For instance, aeration can lead to a reduction of the viscous drag force[23,24], a substantial reduction of the lift force, pitching and yawing-moments, as well as a reduction of the added mass and damping coefficients of the structure[25].

Due to the complexity of the wave breaking phenomenon and the subsequent air entrainment, the void fraction cannot be controlled during wave impacts experiments. Therefore, precise correlations between the initial void fraction and the pressure reduction cannot be deduced easily. In water entry tests is that the initial void fraction in the water tank can be precisely measured and controlled. Therefore, the effect of the aeration on the loads arising during EPL2 process can be quantified and compared to theoretical and or numerical models.

Such impact tests on aerated water are first reported by Eroshin et al. [26–28] who investigated the impact on bubbly water of cones to correlate the maximum impact force with the void fraction. Most other studies found in the literature were conducted with flat plates, and are therefore linked only to EPL1 since these are not water entry tests. Walkden [19] (see also Bullock at al. [22]) conducted drop tests of a flat plate, aiming at quantifying the effects of aeration on wave impacts. In all these cases, the maximum impact force or pressure was shown to decrease with the void fraction, especially for large impact velocities. More recently, Ma et al. [29] and Mai et al. [30] presented experimental investigations of the impact of a rigid square flat plate into pure and aerated water. Their results showed that the peak loading on the plate is reduced to nearly half when the void fraction is only 1.6%. Also, the aeration was shown to increase the rise time of the impact pressure.

Water entry tests of cones on aerated water were only investigated recently by the authors[31]. These tests confirmed the sensible reduction of the impact loads with the aeration, even for low void fractions less than 1%. Indeed, the study reported a reduction of 30% of the impact force when the average void fraction in the impact region was 1.1%. Moreover, their numerical simulations, considering the compressibility of the bubbly mixture, show that the acoustic model used by Eroshin et al. (among others) is valid only when the equivalent Mach number of the mixture is less than 0.3.

The focus of the previous author's study as on the impact force, and pressure evolution of the cone surface was not investigated. The main purpose of the present study is to investigate the influence of impact velocity and aeration on the time evolution of the slamming pressure during a cone water entry. We performed impact tests with a rigid cone with a small deadrise angle ($\beta = 7°$), using a large scale, fully instrumented shock testing hydraulic machine. This unique facility enabled us to keep the impact velocity constant during the impact stage. The instantaneous pressure has been measured at four different locations on the cone surface. The impact tests were done for pure and aerated water entries. The measurement results are presented and analyzed in terms of instantaneous pressure, pressure maxima, pressure

coefficients and pressure impulse. In addition, the expansion velocity of the wetted surface is inferred from the pressure measurements. The Wagner theory (and its extensions) provides a simple model of the pressure signal based on the assumptions of axis-symmetry, incompressibility and self-similarity of the flow around the cone during the slamming event. This model is presented and its predictions are compared to our results from pure water impact tests for three impact velocities. For impacts on aerated water, an aerator was specifically built and laid at the bottom of the water tank beneath the shock machine. Two different void fractions and three different impact velocities were considered. The results are compared to the case of pure water to highlight the influence of the aeration on the instantaneous pressure and the pressure maxima, as well as the pressure impulse.

The remaining of the article is organized as follows. In section 2, the Wagner theory is briefly recalled from which the time evolution of the instantaneous pressure is derived. Section 3 is dedicated to the description of the experimental setup and the instrumentation for the impact tests. In section 4, the impact tests result for pure water are presented and compared to theoretical predictions. The effect of aeration on the impact pressures and pressure impulses is investigated in section 5.

# 2 Hydrodynamic impact models

The impact of a solid body onto the surface of a liquid causes an impulsive motion of the fluid boundary, leading to large pressure gradients and fast local changes in the velocity of the fluid in the vicinity of the impact region. The equations of motion of the fluid are simplified by neglecting viscosity and gravity effects.

The fluid may be considered as incompressible if $p \ll \rho c_0^2$, where $p$ is the pressure, $c_0$ is the speed of sound in the fluid and $\rho$ its mass density. During an impact, the fluid pressure suddenly rises. A pressure of the order of several bars is commonly measured on the surface of the impacting body [12,32]. The pressure maxima are observed near the contact line between the free surface and the body surface. A rapid jet flow appears above the contact line because of the large pressure difference with the surrounding air. Away from the contact line, the free surface rises above its initial position $z = 0$ due to the pressure change in the fluid.

von Karman [4] derived the first expression of the slamming force on a free-falling wedge impacting on a horizontal surface of water for the purpose of designing seaplane floats. The wedge surface lying under the initial free surface is called "wetted surface", its half-width is

denoted by $c$. von Karman's model does not consider the rise of the water surface due to the impact (also called "pill-up" effect). Therefore, the predicted expansion velocity $dc/dt = V_e$ of the wetted surface during the water entry of a wedge or a cone is:

$$V_e = \frac{V_i}{\tan(\beta)} \quad (1)$$

Where $\beta$ is the wedge (or cone) deadrise angle. This expression shows that the expansion velocity could be 10 times larger than the impact velocity for sufficiently small $\beta$ ($\leq 5.7°$). The model in its simplest form neglects the jet flow, and considers the impacting body two-dimensional. The vorticity is conserved during the impact. So, if the fluid is initially at rest, the velocity field during the impact is irrotational and can be defined using a velocity potential $\varphi$. von Karman's model considers only the case of blunt bodies, where the penetration depth is small in comparison with the width of the wetted surface. Therefore, the boundary conditions on the body surface can be projected onto the initial free surface of the fluid ($z = 0$). During the impact, the added mass increases the wedge submergence. By equating the wedge momentum before and after the impact, von Karman derived an expression relating the impact force and the impact velocity.

In the Wagner model, the free surface up-rise (the pill up) is taken into account [5]. We will deal with the specific problem for an axisymmetric cone impacting vertically a still free water surface at a constant velocity $V_i$. In this case, the water flow generated during the cone water entry is considered axi-symmetric and self-similar. The wetted-surface radius $c$ is determined at each time by the geometrical intersection of the free surface and the body surface, the so-called Wagner condition. A consequence of the self-similarity of the flow is that $V_c = dc/dt$ is constant throughout the impact. From the Wagner condition, the following expression of $V_c$ can be derived [33] :

$$\frac{dc}{dt} = V_c = \frac{4}{\pi}\frac{V_i}{\tan(\beta)} \quad (2)$$

The expression of the velocity potential in the contact region is:

$$\varphi = -\frac{2V_i}{\pi}\sqrt{c^2 - r^2} \quad \text{for} \quad r < c \tag{3}$$

Using the linearized Bernoulli equation, $p = -\rho\, \partial\varphi/\partial t$, the following expression of the pressure distribution on the wetted surface is obtained:

$$p(r,t) = \frac{2}{\pi}\rho V_i V_c \left(1 - \frac{r^2}{c(t)^2}\right)^{-\frac{1}{2}} \quad \text{for} \quad r < c \tag{4}$$

Denoting by $t_c$ the time at which the wetted surface first reaches the radial position $r$, $t_c = r/V_c$, Eq. (4) can be rewritten in the following form:

$$p(r,t) = \frac{2}{\pi}\rho V_i V_c \left(1 - \frac{t_c^2}{t^2}\right)^{-\frac{1}{2}} \quad \text{for} \quad t > t_c \tag{5}$$

This equation predicts that the pressure at a given position will decrease continuously with time when $t > t_c$. The asymptotic pressure for large times $t \to +\infty$ is independent from $r$ and is equal to $2/\pi\, \rho V_i V_c$ .

This expression is singular at the time of the first contact $t_c$, where the model predicts an infinite pressure. In order to determine the peak pressure acting on the impacting body, Wagner [5] developed a local two-dimensional solution for the jet flow at the vicinity of the boundary of the contact surface. He showed that the peak pressure is related to the expansion velocity of the wetted surface:

$$p_{max} = \frac{1}{2}\rho V_c^2 \tag{6}$$

Using matched asymptotic expansions, Zhao and Faltinsen [6] proposed a composite formulation that provides a regular and continuous pressure distribution on the whole contact surface. This

model was initially dedicated to two-dimensional problems. Its extension to the axisymmetric case was proposed by Scolan [34]. The pressure distribution reads:

$$p(r,t) = \frac{2\rho c V_i V_c}{\pi\sqrt{c^2-r^2}} - \frac{2\rho c V_i V_c}{\pi\sqrt{2c(c-r)}} + 2\rho V_c^2 \frac{\sqrt{\tau}}{(1+\sqrt{\tau})^2} \quad \text{for } r < c(t)$$
$$p(r,t) = 2\rho V_c^2 \frac{\sqrt{\tau}}{(1+\sqrt{\tau})^2} \text{ for } r \geq c(t) \tag{7}$$

where $\tau$ is a positive real number given by the following equation:

$$r - c = \frac{\delta}{\pi}\left(-\ln(\tau) - 4\sqrt{\tau} - \tau + 5\right) \text{ with:} \qquad \delta = \frac{V_i^2 c}{2\pi V_c^2} \tag{8}$$

Another model for the pressure distribution is the Modified Logvinovich model proposed by Korobkin [7]. The pressure on the wetted surface is given by the following expression:

$$p(r,t) = -\rho\left[\psi_{,t} + \frac{f_{,r}V_i}{1+f_{,r}^2} + \frac{1}{2}\frac{\psi_{,r}^2 - V_i^2}{1+f_{,r}^2}\right] \text{ with:}$$
$$\psi = \varphi^{(w)} - V_i\big(f(r) - h(t)\big) \tag{9}$$

Where $\varphi^{(w)}$ is the Wagner velocity potential, given by Eq. (3). Results derived from the Wagner model, the Zhao and Faltinsen model (ZF) and Modified Logvinovich model (MLM) are presented and compared to experimental data in section 4 in the case of pure water.

# 3 Experimental set-up and techniques

## 3.1 The hydraulic shock machine

The experiments were performed using a large-scale hydraulic shock machine (SERVOTEST) shown in Fig. 1-a. The impacting solid was a rigid cone made of aluminum alloy 7075 of diameter $D$ = 33 cm and dead-rise angle of $\beta = 7°$ (Fig. 1-b)). The dimensions of the cone are

shown in Fig. 1-c. The cone was attached to the end of the piston of the shock machine. The main advantage of this machine is that it permits to maintain a nearly constant velocity during the impact. The machine consisted of a double acting hydraulic cylinder. The cylinder barrels and the piston are enclosed inside the machine. The oil is pressurized by an external pump and kept at a high pressure in the accumulators. These are located on the upper side of the cylinder and are visible in Fig. 1-a. The piston is set into motion when the pressure is released. The flow rate of oil from the accumulators into the cylinder is regulated by several servo-valves. The velocity of the piston is proportional to the oil flow rate in the cylinder. The reference velocity and the expected maximum force are set by the user prior to the impacts. From this, the machine computer calculates the time profile of the oil flow rate, and sets the time sequence of the activation of the servo-valves during the test. The machine can deliver a translation velocity up to 20 m/s when the maximum load is less than 100 kN, or 10 m/s when the maximum load is between 100 kN and 200 kN [11].

**(a)**


**(b)**

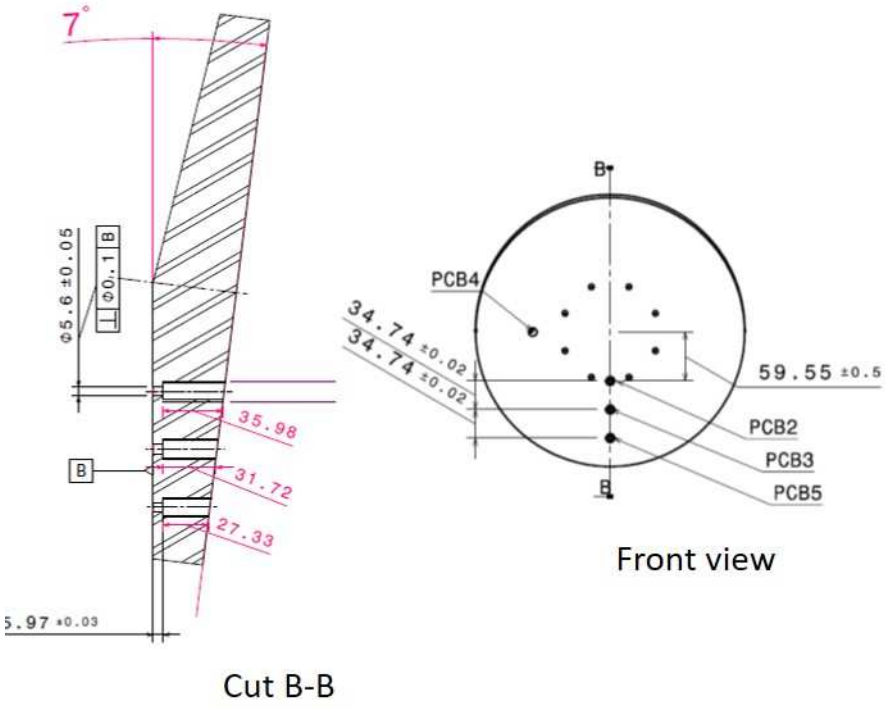


**(c)**

*Figure 1. Experimental setup: (a) the shock machine, (b) the steel cone used in the experiments, attached to the shock machine piston, (c) dimensions (in mm) of the cone and positions of the pressure sensors (PCB).*

## 3.2 Instrumentation

The cone acceleration was measured by a piezo-resistive accelerometer screwed to the cone upper surface. The accelerometer measuring range is $\pm 250$g and its sensitivity is 0.32 mV/g. Based on the device sensitivity, the uncertainty on acceleration measurement is estimated to be $\pm 0.12$ g. The cone vertical velocity $V_i$ was computed by integration of the acceleration signal in time [11]. Examples of the evolution of the impact velocity with time are shown in Fig. 2, where the

instantaneous velocity is normalized by the test reference impact velocity. In this study, we report impact tests with three reference velocities: $V_i$= 5, 7 and 9 m/s. The velocity first increases and reaches the reference value. Then it stays nearly constant for more than $10^{-2}$s. During this period, the cone velocity may vary within ±4% of the reference velocity. The time between the first contact with the free surface and the full immersion of the cone is set within this period. An electrical contact sensor was used to detect the time of the first contact between the cone tip and the water surface [11,32]. When the cone tip first touches the water surface, the tension from the electrical contact sensor rises. This time will be considered as the reference time $t$=0 in the following. The uncertainty on the time of the first contact is estimated as $10^{-5}$s, which is the observed rise time of the tension from the sensor.

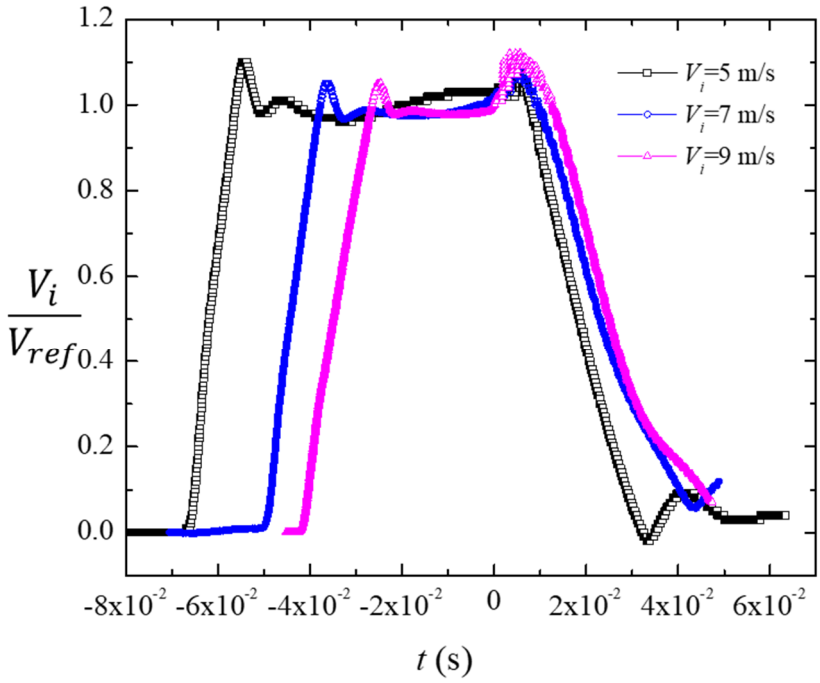


*Figure 2. Examples of time evolutions of the normalized entry velocity for several reference velocity. The normalized entry velocity is the ratio of the cone velocity over the reference impact velocity.*

We measured the instantaneous pressure at four different locations of the surface of the cone, shown in Fig. 1. Piezoelectric pressure transducers from PCB Piezotronics (USA) were used. All sensors were flush mounted onto the surface of the cone, so that the sensing surfaces are directed towards the water surface. The sensing area diameter is 5.54 mm. These sensors could measure dynamic pressures up to 2758 kPa with a sensitivity of 3.6 mV/kPa, its resonant frequency is larger to 500 kHz and rise time lower to 1.0 µs.

The sensors positions on the surface of the cone are shown in Fig. 1-c. Three sensors PCB2, PCB3 and PCB5 were at the same angular position, while at different radial positions $r_2 = 0.36 \times D/2$, $r_3 = 0.57 \times D/2$ and $r_5 = 0.78 \times D/2$, respectively. The sensor PCB4 was installed at the same radial position as PCB3 but at an angle of 90° from PCB3.

The signals from all the measuring devices were acquired and conditioned by means of an "LDS Nicolet Genesis" acquisition system. Differential input technique was used in order to mitigate the electromagnetic interferences noise. All signals were sampled simultaneously at a frequency of 100 kHz. Each acquisition was triggered when the first contact between the cone tip and the water surface occurred. Sweep recording enables recording data before and after the first contact, with a total recording time of 2 s, including the impact duration.

### 3.3 Aeration

For the purpose of air bubble generation, an aerator was installed in the bottom of the water tank. The inner dimensions of the tank are 2 m wide and 3 m long with a maximum depth capacity of 2 m. The water level was set at 1.2 m to allow impacts for all tests. The air supply system, as well as the associated instrumentation, are the same as used in a previous work by the authors [31] to study the influence of aeration on the global impact force. It was made of an array of 30 parallel porous soaker hoses. The hoses array spans the width of the tank. Compressed air was injected at both ends of each hose. The total air mass flow rate was monitored using two rotameters connected in parallel. The injection pressure was controlled using a pressure regulator and measured by a digital manometer. The uncertainty in the measurement of the mass flow rate is $\pm$ 2.5 $L_{std}$/min while that in the air pressure measurement is $\pm$0.01 bar, where $L_{std}$/min stands for standard liter per minute unit. The impact tests reported in the present study were performed for two different values of the air mass flow rate $Q =$ 108.3 and 327 $L_{std}$/min.

Prior to the impact tests, the spatial distribution of the local void fraction of the bubble plume has been characterized by the use of an optical probe [31]. In the first 10 cm beneath the free surface, the spatial homogeneity of the time averaged void fraction was checked: the maximum relative variation in local void fraction is expected to be ±20%. A linear evolution of the time averaged void fraction with the air injection rate was observed, thus making possible to conclude that the bubble rising velocity is $V_b \approx 20$ cm/s approximately, regardless of the injection rate. This velocity is in agreement with the terminal velocity of spherical bubbles of

mean diameter $d_b$ ≈1.3 mm, which is in the range of the bubble sizes [1 mm - 2 mm] measured in a bubble plume generated by the same soaker hoses [35].

For the sake of simplicity, only the spatial and time averaged void fraction (mean void fraction $\alpha_0$ measured in the first 10 cm beneath the free surface) has been considered for each mass flow rate. The relative uncertainty in the measurement of $\alpha_0$ is 10%, which takes into account both the size of the tips of the optical probe and the sampling frequency of the optical measurement system. The mean void fraction increases linearly with the flow rate from $\alpha_0 = 0.35\%$ for $Q = 108.3\ \mathrm{L_{std}/min}$ to $\alpha_0 = 1.1\%$ for $Q = 327\ \mathrm{L_{std}/min}$.

The bubble plume induced velocity of the liquid can be estimated through a three fluids model[36]. In this approach, the vertical induced velocity of the liquid can be written as: $V_L \approx ((1-\alpha_0-C_a\alpha_0){V_L}^0 + C_a\alpha_0 V_b)/(1-\alpha_0)$ where $C_a$ denotes the added mass coefficient of the bubbles ($C_a \approx 0.5$), $C_a\alpha_0$ is the relative volume of liquid driven by the bubbles at their terminal rising velocity $V_b$. ${V_L}^0$ represents the undisturbed volume of the liquid, which is zero in the tank. Considering both the values of $V_b$ and the values of the averaged void fraction at stake $\alpha_0$, the bubble plume induced velocity of the liquid is very small (less than 0.2 cm/s), compared to the impact induced velocities and are expected to have no effect.

The relaxation time of the bubbles varies with the bubble size $d_b$, an estimate is given by [21] : $\tau_b \approx {d_b}^2/18\,\nu = 5\times10^2 s$, with ν the kinematic viscosity of the water. An estimate of the Stokes number is $St = \tau_b/\tau_{impact}$, with $\tau_{impact} = D/2V_c$ being the time duration of an impact. This leads to $St$ number values larger than 14 for the different impact velocities. The Reynolds number based the fluid flow (induced by the impact) and the bubble size, $V_c.d_b/2\nu$, is larger than $3\times10^4$ and the size parameter $d_b/D$ is about $4\times10^{-3}$. The values of these characteristic numbers indicate the motion of the bubbles, relative to the fluid, during the impact stage will be negligible, meaning that the bubbles are advected with the water during an impact (see Brennen's book [21], section 2.4.2 for more details).

# 4 Effect of the impact velocity (impacts on pure water)

In this paragraph, the pressure distribution on a cone during its vertical penetration into pure water is characterized experimentally for 3 impact velocities: 5, 7 and 9 m/s. In addition, the relationship between the expansion velocity of the wetted surface and the impact velocity is determined.

## 4.1 Visualization of the cone water entry

Several aspects of the hydrodynamic impact phenomena may be revealed through flow visualization. To that end, the water entry of the cone was visualized using a PHOTRON high-speed camera at 20000 frames per second. For the purpose, the water tank has large windows on its four sides, providing optical access. The high-speed camera was fixed on a tripod and placed on one side. A powerful light projector was placed on the opposite side in order to provide enough light for imaging. The camera rotation and tilt were carefully tuned in order to make its optical axis perpendicular to the plane of the window. Imaging was performed only in the case of pure water, because the bubbles in the case of aerated water would significantly attenuate lighting intensity, yielding dark images that are unfit for visual inspection.

Examples of the acquired images are shown in Fig. 3 for an impact test on pure water at $V_i = 9$ m/s. Images from the other tests share the same features and are not presented here, but can be found in the video sequences provided as supplementary material. The images are presented in time-ordered fashion, and each image is shown with its time tag. The shadows of all the objects obstructing or deviating light paths between the light source and the camera are visible in the images. This includes the cone; the shock machine cylinder and the wires and screws used to fix and connect the instruments (Fig. 3a). Initially, the free surface seems blurred and cannot be clearly distinguished. As the free surface slightly rises during the impact, the light rays crossing it are deviated. This leads to the appearance of a dark line at the position of the free surface (Fig. 3b).

Below the free surface, the cone surface seems to be surrounded by a thin cloud of small air bubbles (Fig. 3c). Few isolated bubbles that moved away from the cloud can be clearly distinguished. Their size is estimated by visual inspection as less than 5 mm. Some of the air could not escape freely, thus creating free-surface instabilities leading to the appearance of these entrained bubbles near the interface. This phenomenon is referred to as “air entrainment” in the literature. It is distinct from the “air entrapment” which involves larger air pockets and occurs for smaller deadrise angles ($\beta < 3°$) [37]. The wetted surface can be clearly distinguished in the images (Fig. 3b), so that it’s the width $c$ and length $h$ can be estimated for each image with reasonable accuracy. From Wagner’s theory, the ratio $c/h$ (with $h$ the cone penetration depth) is constant and equal to ratio $V_c/V_i$. Interestingly, the ratio $c/h$ was estimated between 9 and 12, which is reasonably close to the value 10.39 from the theory Eq. (2). Finally, after the cone is fully immersed (i.e. when the water reaches the first knuckle) a splash appears and partially obstructs the field of view (Fig. 4d).

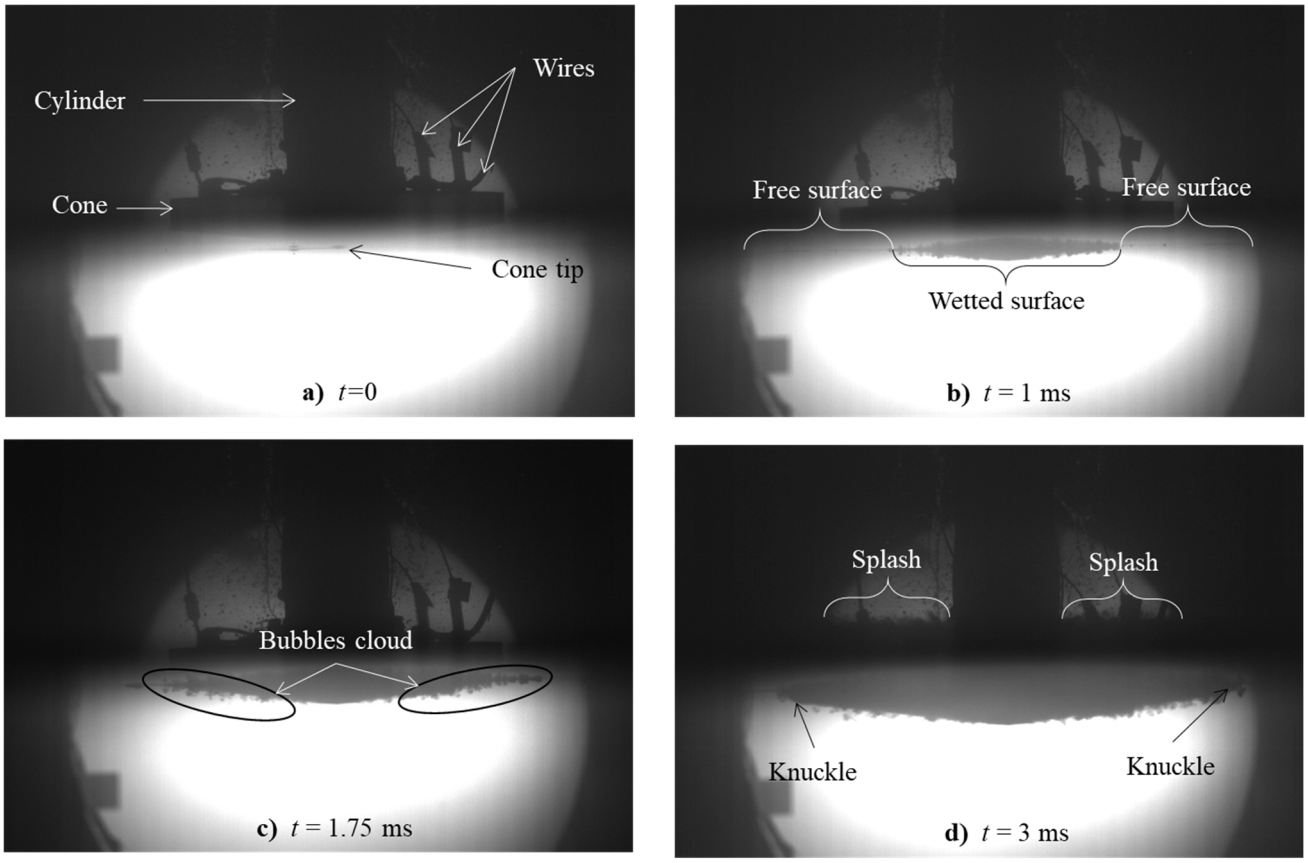


*Figure 3: Time-ordered pictures of the cone water entry stage for an impact velocity Vi=9 m/s. (a) first contact between the cone apex and the water surface, (b) cone partially immerged, (c) cone nearly fully immerged, (d) appearance of the splash after the full submergence of the cone surface.*

## 4.2 Analysis of the impact pressure signals

We will now examine the pressure signals from the PCB sensors, in order to describe how the pressure on the cone surface evolves during the impact. Examples of instantaneous pressure signals $P_2$, $P_3$, $P_4$ and $P_5$ obtained from pressure taps PCB2, PCB3, PCB4 and PCB5, respectively, are shown in Fig. 4 for $V_i$ =5, 7 and 9 m/s. We recall that the reference time $t = 0$ is the time of the first contact between the cone tip and the water surface (see Fig. 3 a)). Clearly all the pressure signals have the same shape, albeit being delayed in time. These signals can be divided into four different stages with distinct features.

During the first stage, the sensor is above the free-surface and the pressure on the sensor is zero. The second stage begins at the first contact between the sensor and the free surface. That is when the contact line reaches the position of the sensor. The pressure suddenly rises and reaches its maximum (see Fig. 4b). The "rise time" is defined as the duration of this rising edge, i.e., the time during which the pressure rises from zero to the first peak. The rise time is very

short and decreases with the increase of the velocity. For PCB2, it is about 0.12 ms when $V_i = 5$ m/s and 0.05 ms when $V_i = 9$ m/s.

The contact line first reaches PCB2 then PCB3 and finally PCB5. The rising edges in $P_3$ and $P_4$ occur almost simultaneously, meaning that the contact line reaches PCB3 and PCB4 at the same time. This shows that the expansion velocity of the wetted surface is independent of the angular position, a consequence of the axis-symmetry of the flow around the cone. The pressure reaches its maximum value at the end of this stage. The recorded maxima are quite large, and depend on the impact velocity: they reach $\sim 8 \times 10^5$ Pa (8 bar) when $V_i = 5\ m.s^{-1}$ and $\sim 25 \times 10^5$ Pa (25 bar) when $V_i = 9$ m/s. During each test, the pressure maximum often differs significantly from one sensor to the other: the difference between the maxima of $P_3$ and $P_4$ exceeds $2 \times 10^5$ Pa for $V_i = 5$ m/s (Fig. 4a), and the difference between the maxima of $P_2$ and $P_4$ exceeds $7 \times 10^5$ Pa for $V_i = 7$ m/s (Fig. 4b).

The third stage lies between the occurrence of the pressure peak and the full immersion of the cone (Fig. 4c). It is the part of the signal that will be used for comparison with the theory presented in section 2. During this stage, the pressure declines gradually as the contact line travels away from the sensor and the contact surface continues to expand. Finally, the fourth stage begins when the cone is fully immersed. The contact surface expansion stops, as a result the pressure from all sensors vanish simultaneously and quickly (e.g., for $t > 2$ ms at $V_i = 9m.s^{-1}$ in Fig. 4c). This is concomitant with the appearance of the splash (Fig. 3d). This stage signals the end of the impact event as considered in the theoretical models, and therefore will not be studied here.

Relatively small pressure fluctuations (or ripples) are observed on these signals during the third stage. These are likely due to the pulsation of the small bubbles entrained during water entry. From the three graphs in Fig. 4, we can estimate the period of the pressure fluctuations to a few tenth of milliseconds. Moreover, the fluctuation period seems to slightly decreases with the impact velocity. Let us show that this might be the pulsation frequency of the entrained bubbles. The natural pulsation frequency of a spherical bubble is derived from the Rayleigh-Plesset equation [38]. This frequency depends on the size of the bubble and the pressure of gas inside the bubble. In the impact region, this pressure must be of the order of $10^5$ Pa (see Fig. 4). The entrained bubbles size is likely to be about $10^{-3}$ m. From these values, we obtain a natural bubble period of $3 \times 10^{-4}$ s, which is consistent with the period of the pressure fluctuations.

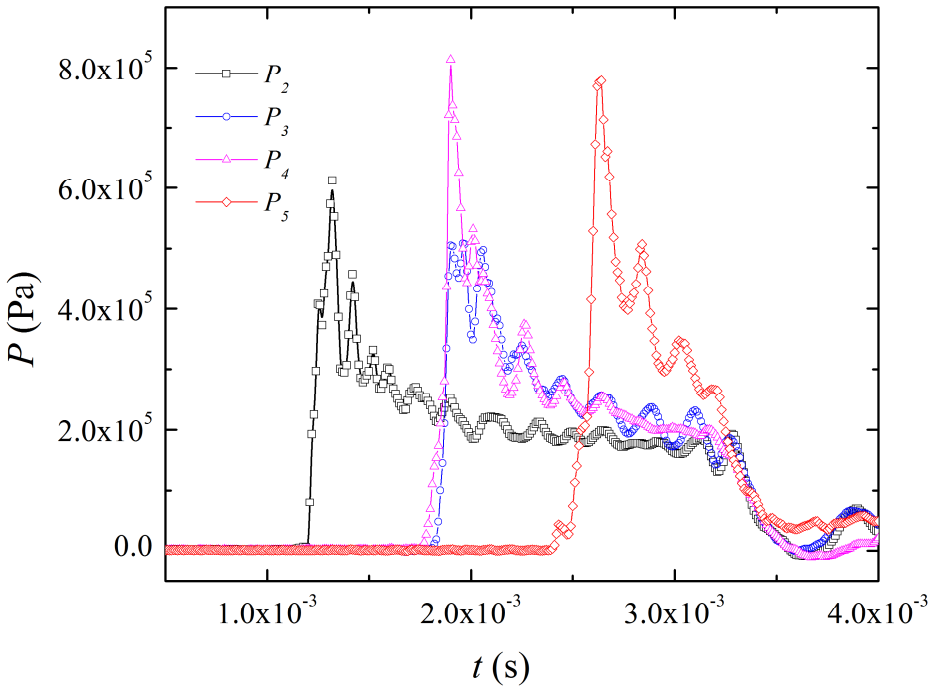
8.0x10^5
6.0x10^5
4.0x10^5
2.0x10^5
0.0
P (Pa)
P_2
P_3
P_4
P_5
1.0x10^-3
2.0x10^-3
3.0x10^-3
4.0x10^-3
t (s)

**(a)**

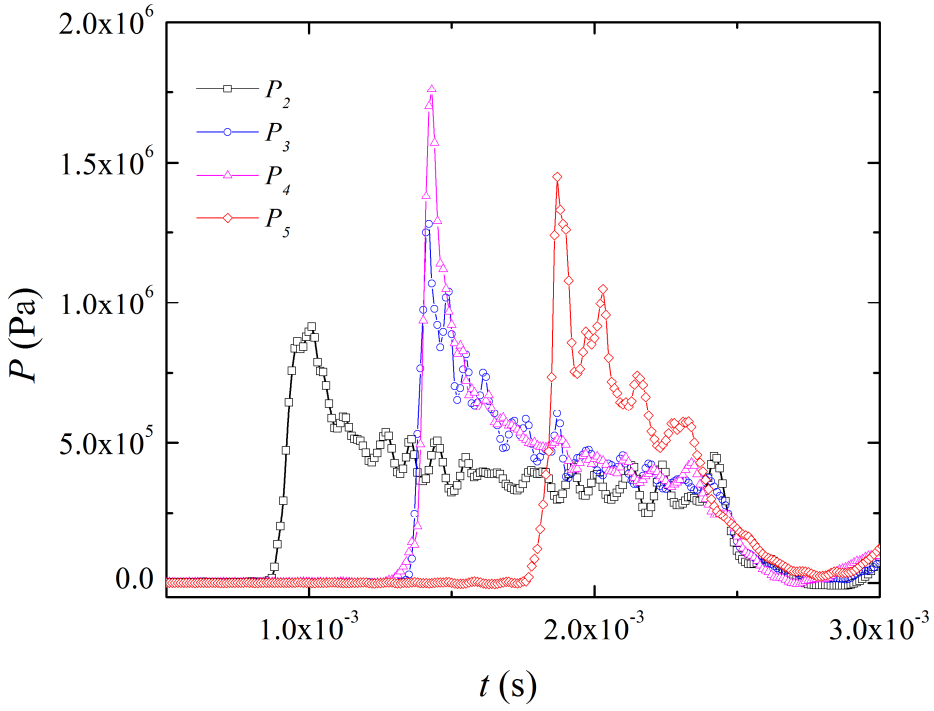
2.0x10^6
1.5x10^6
1.0x10^6
5.0x10^5
0.0
P (Pa)
P_2
P_3
P_4
P_5
1.0x10^-3
2.0x10^-3
3.0x10^-3
t (s)

**(b)**

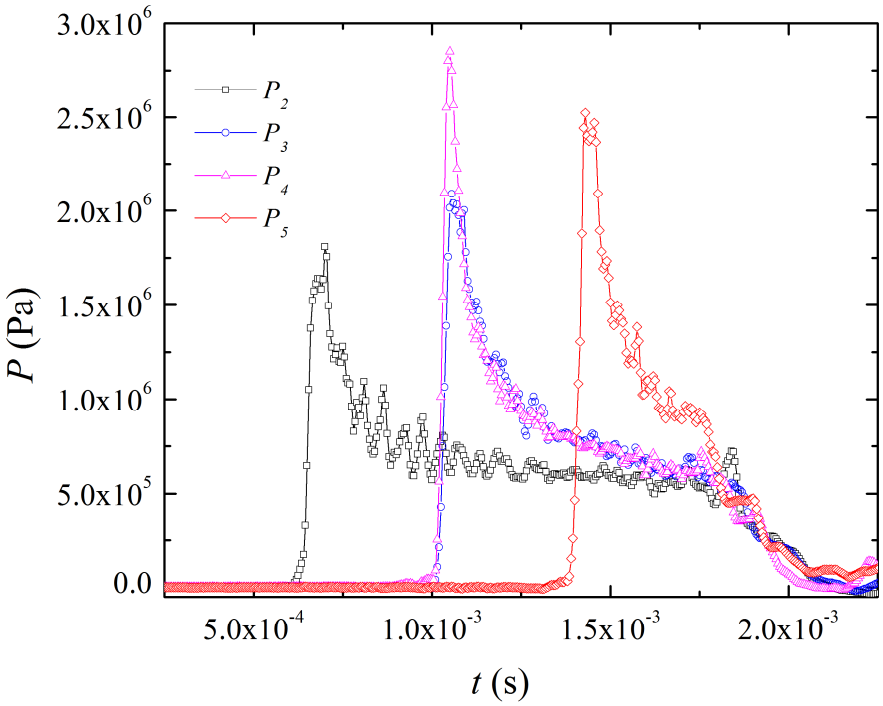


**(c)**

*Figure 4. Examples of instantaneous pressure signals from the four pressure sensors for pure water at three different impact velocities, (a) $V_i$=5 m/s, (b) $V_i$=7 m/s, (c) $V_i$=9 m/s. For clarity, symbols are shown every 10 samples.*

Finally, we checked the repeatability of the pressure measurements in Fig. 5, where pressure signals obtained from different tests at the same impact velocity are compared. A good match between the curves is observed, with the rising edges of the pressure occurring at almost the same time. Beyond the jumps, the values of the pressure from the two tests are very close to each other. This was confirmed for all other impact tests. However, the values of the maximum pressure differ from one test to the other, meaning that the pressure peak measurements are not repeatable. In a previous study [32], pressure measurements were carried out during the impact of a square pyramid with a deadrise of 14°. The experimental set-up was very similar to the one of the present study (in particular, the same pressure sensors and data acquisition system were used). El Malki et al. [32] observed that the peak pressure measurements were almost repeatable. In the present case, larger differences in peak pressures between different tests are observed. It is difficult to conclude about the cause of this scatter. However, it should be noted that the cone considered in the present study has a smaller deadrise angle (7°). For this reason, the typical duration of the pressure peak is smaller (for a given impact velocity) and therefore the maximal pressure is more difficult to capture. Moreover, the presence of entrapped air

bubbles, observed from high-speed imaging (see section 4.1), may generate some disturbance of the pressure field and contribute to make the pressure measurements less repeatable.

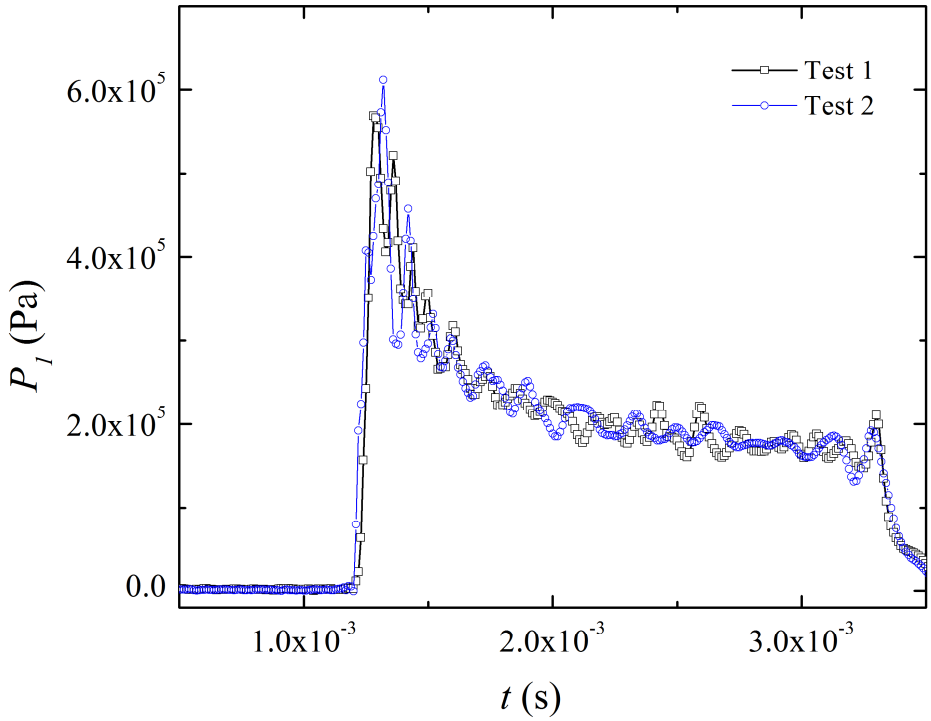


**(a)**

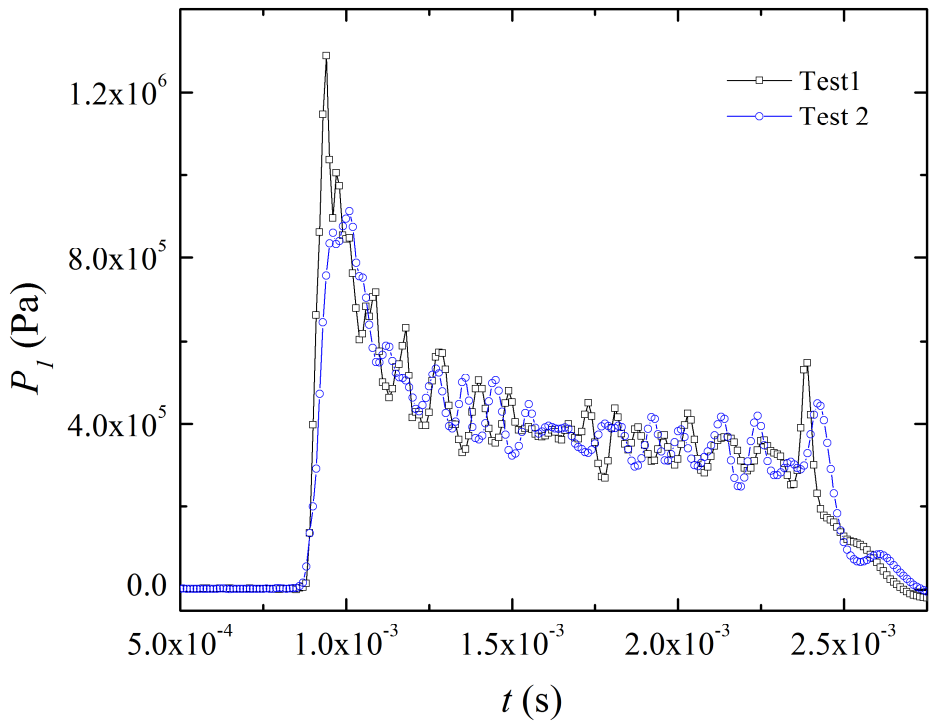


**(b)**

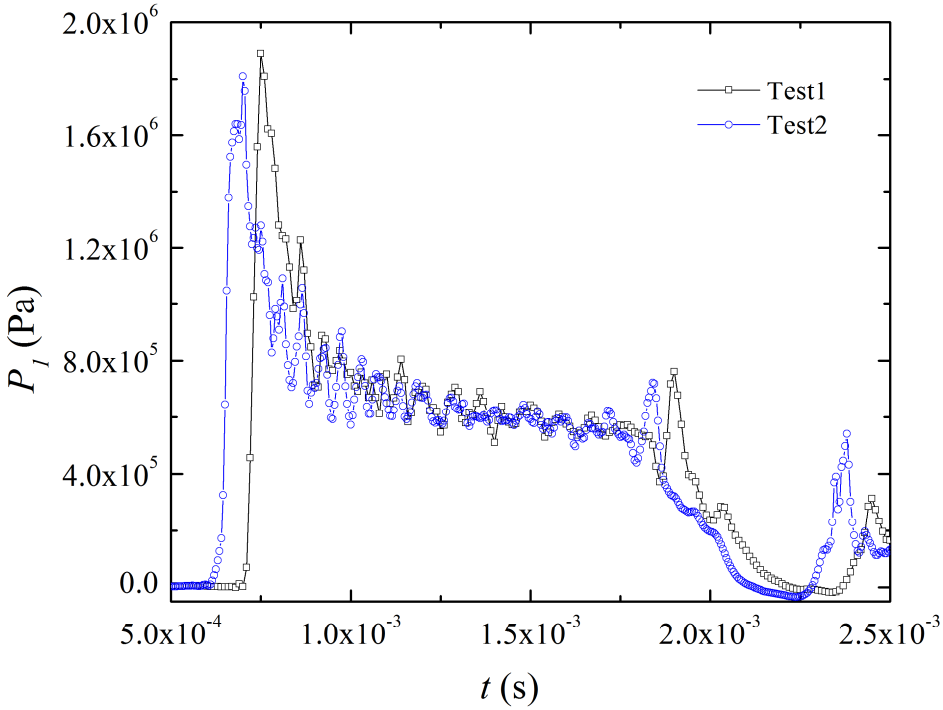


**(c)**

*Figure 5. Comparison of the instantaneous pressure signals from the same sensor (PCB2) and from different tests on pure water at the same impact velocity: (a) $V_i$=5 m/s, (b) $V_i$=7 m/s, (c) $V_i$=9 m/s.*

## 4.3 Expansion velocity of the wetted surface

The expansion velocity $V_c$ defines how fast the contact surface between the solid and the liquid grows during the impact. As shown in the second section, the Wagner theory (through the Wagner condition) provides a linear relation between $V_c$ and $V_i$ and suggests a link between $V_c$ and the impact pressure values and evolution. Indeed, the pressure maximum and asymptotic values, as well as how fast the pressure decreases with time are all function of $V_c$ (see Eqs. (6) and (4), respectively). Therefore, the expansion velocity is a key parameter for describing the hydrodynamic impact phenomena. However, to the authors' best knowledge, measurements of this quantity for a cone are lacking in the literature. Here we aim at quantifying the expansion velocity from the pressure signals.

The pressure signal increases stepwise immediately after the first contact between the sensor surface and the free surface. For pressure sensor number $n$, the time of the first contact $t_{cn}$ is the time when the pressure jump occurs. Practically, it is defined as the time when the pressure signal first reaches $10^5$ Pa. Let $r_n$ be the radial position of the sensor number $n$, an estimate of the average expansion velocity between $t = 0$ and $t_{cn}$ is $V_c = r_n/t_{cn}$. The precision of this

estimation is affected by the uncertainty on $t = 0$ through $t_{cn}$. In order to remove the influence of this uncertainty, we will consider instead the average $V_c$ *between* pressure sensors (having the same angular position). From the signals of the three pressure sensors PCB2, 3 and 5, two independent estimates of $V_c$ are considered:

$$V_{32} = \frac{(r_3 - r_2)}{t_{c3} - t_{c2}}$$
$$V_{53} = \frac{(r_5 - r_3)}{t_{c5} - t_{c3}} \qquad (10)$$

Considering the sensor PCB4 instead of PCB3 gives fairly the same values of $V_c$ because the difference between $t_{c3}$ and $t_{c4}$ is relatively small (on average $t_{c4} - t_{c3} = 2.5 \times 10^{-5}$s). A third possible estimator, $V_{52} = (r_5 - r_2)/(t_{c5} - t_{c2})$, is not independent since it can be written as a function of $V_{32}$ and $V_{53}$. The uncertainty on these estimates comes from the uncertainty on the time and position differences. From the geometrical tolerances in Fig. 1, the uncertainty on the position differences ($r_3 - r_2$, $r_5 - r_3$ and $r_5 - r_2$) is estimated at $\pm 0.02$mm (or 0.06%) and is neglected. The time differences ($t_{c3} - t_{c2}$, $t_{c5} - t_{c3}$ and $t_{c5} - t_{c2}$) are not affected by the time of the first contact $t = 0$, the uncertainty is related to the time resolution of the signal and is estimated at $\pm 10^{-5}$ s (the sampling period). The resulting uncertainty on these estimators of $V_c$ is therefore less than $\pm 2.7\%$.

The values of the estimates of $V_c$ as a function of $V_i$ are shown in Fig. 6. We present $V_{32}$ and $V_{53}$ against $V_i$ (almost constant for each test). The figure also shows the theoretical predictions from the Wagner model (straight line). The results are also reported in Table 1 for each impact test. One observes that the values of $V_{32}$ and $V_{53}$ are well repeatable between the different tests. Indeed, the discrepancy between two different tests is less than 7.7% for $V_{32}$ and 10.4% for $V_{53}$. These discrepancies are not well correlated with the slight variation $V_i$ between different tests. They are most likely caused by small changes of the experimental conditions, including the free surface roughness and bubbles entrainment. The values of $V_{32}$ and $V_{53}$ are fairly close, with a discrepancy smaller than 10 %. This observation shows that the expansion velocity is fairly constant during the impact, a consequence of the self-similarity of the flow around the cone and the steadiness of the impact velocity.

Most importantly, Fig. 6 clearly shows that the values $V_{32}$ and $V_{53}$ are in good agreement with the Wagner theory. This shows that the $V_c$ can be accurately inferred from multiple pressure transducers signals. It is worth noting that this method can easily be applied to more complex geometrical configurations of water entry, where $V_c$ is unsteady (e.g. impact of a hemisphere) or non-uniform (e.g. when the geometry is not two-dimensional or axisymmetric). In these cases, a larger number of pressure transducers will be needed in order to accurately track the time and space variations of $V_c$. This method may also be extended to other hydrodynamic impact configurations, including wave impact on a wall.

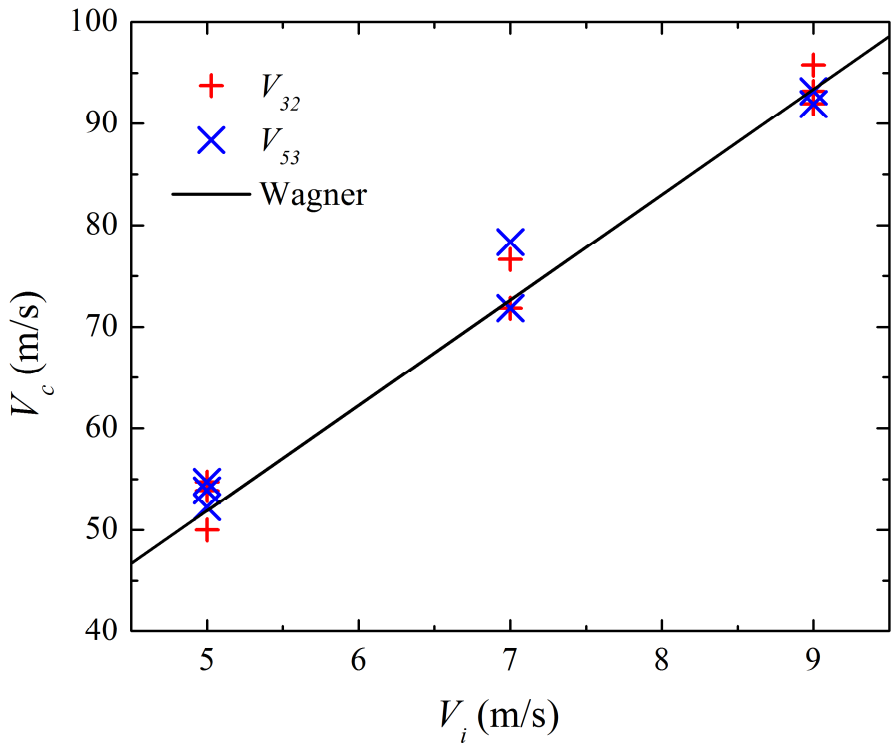


*Figure 6. Expansion velocity estimates, $V_{32}$ and $V_{53}$, for all impact tests on pure water as a function of the impact velocity $V_i$. The experimental results are compared to the predictions of the Wagner theory.*

| Test | $V_i(t_{c3})$ (m/s) | $V_{32}$ (m/s) | $V_i(t_{c5})$ (m/s) | $V_{53}$ (m/s) |
|---|---|---|---|---|
| V5_T1 | 5.18 | 51.09 | 5.16 | 54.28 |
| V5_T2 | 5.12 | 54.28 | 5.09 | 53.45 |
| V5_T3 | 5.17 | 54.28 | 5.14 | 55.14 |
| V5_T4 | 4.89 | 55.14 | 4.86 | 50.35 |
| V7_T1 | 7.23 | 78.95 | 7.20 | 72.38 |
| V7_T2 | 7.46 | 73.91 | 7.44 | 80.79 |
| V7_T3 | 7.07 | 77.20 | 7.03 | 78.95 |
| V9_T1 | 9.21 | 96.50 | 9.18 | 91.42 |
| V9_T2 | 9.08 | 89.08 | 9.07 | 93.89 |
| V9_T3 | 8.95 | 95.18 | 8.96 | 93.89 |

*Table 1: Values of the expansion velocity estimators $V_{32}$ and $V_{53}$ as a function of the instantaneous impact velocity $V_i(t_{c3})$ and $V_i(t_{c5})$ respectively for all impact tests on pure water.*

## 4.4 Pressure coefficient profiles

Let us consider the pressure signal at any radial position $r$ of the cone. Assuming that the influence of liquid viscosity and compressibility is negligible, because of the symmetry of the flow around the $z$-axis, dimensional analysis demonstrates that the pressure coefficient $C_p = 2\,p/\rho V_i^2$, at a given radial position $r_i$, depends only on the dimensionless time $t^* = tV_e/r_i$. From the Wagner model, this coefficient can be written as:

$$C_p(t^*) = \frac{4}{\pi}\frac{V_c}{Vi}\left(1 - \frac{t_c^{*2}}{t^{*2}}\right)^{-\frac{1}{2}} \qquad \text{for} \qquad t^* > t_c^* \tag{11}$$

where

$$t_c^* = \frac{t_{ci}V_e}{r_i} = \frac{\mathrm{V_e}}{\mathrm{V_c}} = \frac{\pi}{4} \approx 0.78$$

is the normalized time of the first contact with the free surface at position $r_i$. The relationship between $C_p$ and $t^*$ is independent of the instantaneous impact velocity $V_i$ and the fluid density $\rho$. For a large $t^*$, the pressure coefficient reaches the asymptotic value:

$$C_p(\infty) = \frac{4}{\pi}\frac{V_c}{Vi} = \left(\frac{4}{\pi}\right)^2 \frac{1}{\tan(\beta)} \qquad (12)$$

In Fig. 7, we examine the evolution of $C_p$ with $t^*$ for all the four sensors during the same impact tests, and for three different impact velocities. A good match between all curves is observed before the full immersion of the cone, also for all other impact tests (not shown). For all sensors, the rising edges appear close to $t^* = 0.8$, where the rapidly increasing $C_p$ reaches its maximum, larger than $C_p = 40$. The $C_p$ maximum values are not repeatable, being considerably scattered for different sensors. After reaching its maximum, the $C_p$ decreases slowly up to the time of full immersion. In this time interval, the values of $C_p$ for different sensors are fairly close to one another. This confirms the axis-symmetry and self-similarity hypotheses are well verified during the impact. Because the recording duration of the sensors is different, the non-dimensional time of full immersion varies. The longest recording (PCB2) shows that the pressure coefficient eventually reaches values between 10 and 15 at $t^* = 2$ which is close to the asymptotic value of $C_p(\infty) = 13.2$ from the Wagner theory. Fig. 8 presents pressure coefficient profiles recorded at the sensor PCB2 during three tests with different impact velocities (5, 7 and 9 m/s). It is observed that the evolution of $C_p$ with $t^*$ is independent of the impact velocity, indicating that compressibility effects have no influence on impacts on pure water.

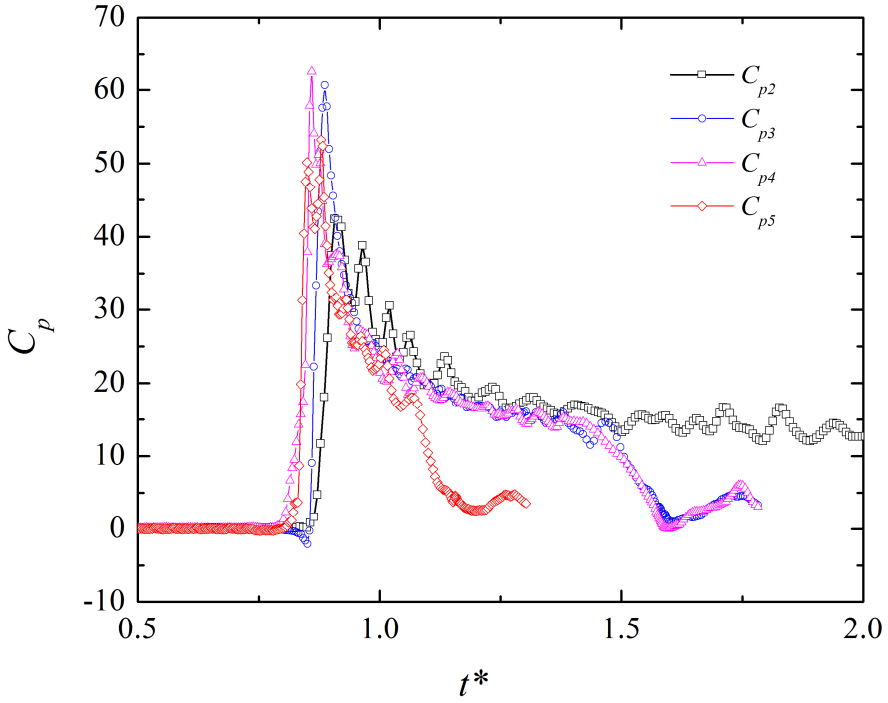
70
60
50
40
30
20
10
0
-10
0.5
1.0
1.5
2.0
$C_p$
$t^*$
$C_{p2}$
$C_{p3}$
$C_{p4}$
$C_{p5}$

**(a)**

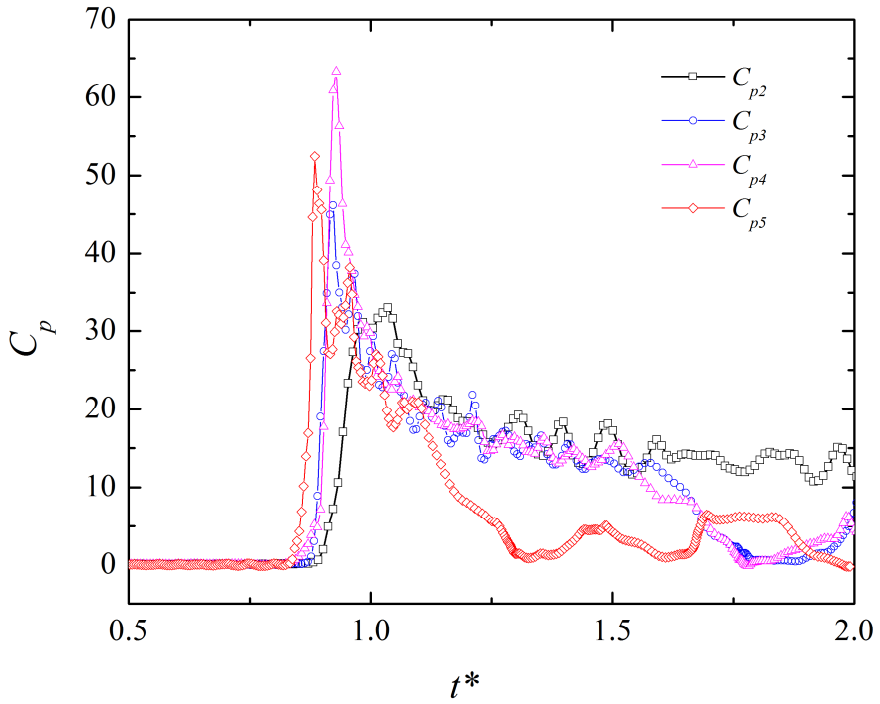
70
60
50
40
30
20
10
0
0.5
1.0
1.5
2.0
$C_p$
$t^*$
$C_{p2}$
$C_{p3}$
$C_{p4}$
$C_{p5}$

**(b)**

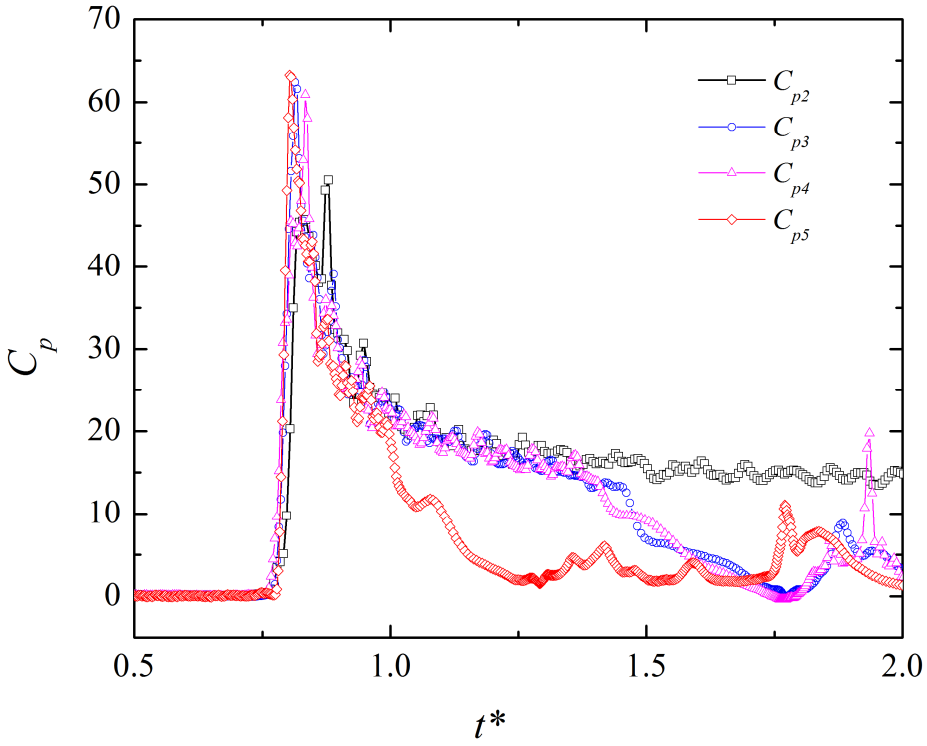


**(c)**

*Figure 7. Evolution of the pressure coefficient $C_p$ with normalized time t* from the four sensors during impact tests on pure water performed at different impact velocities: (a) $V_i$=5 m/s, (b) $V_i$=7 m/s, (c) $V_i$=9 m/s.*

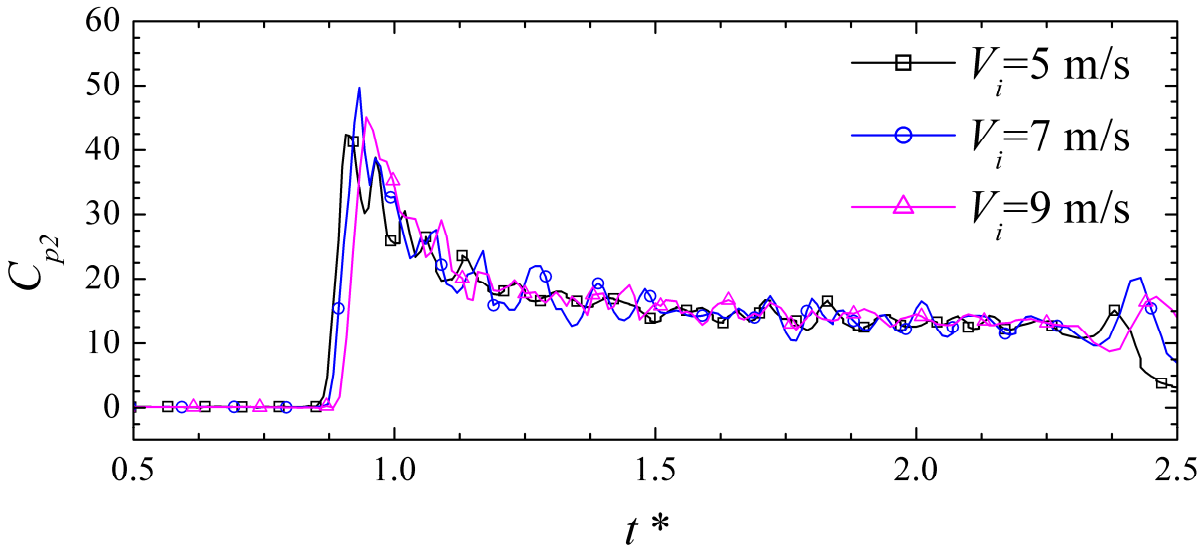

*Figure 8. Comparison between pressure coefficient $C_p$ profiles from the sensor PCB2 recorded during three tests with different impact velocities.*

Fig. 9 presents a comparison between an experimental pressure coefficient profile (from the sensor PCB2) and the predictions of the Zhao and Faltinsen model (ZFM) and the Modified Logvinovitch model (MLM). As explained in section 2, the advantage of the ZFM and MLM over the original Wagner model is that they predict a finite value of the pressure at the time of first contact. It is known that measurements of pressure peaks can affected by the size of the active area of sensor [39]. The sensors used in the present experiments have a circular active area with a diameter of 5.54 mm. Therefore, using the Zhao and Faltinsen model and the MLM, we have computed the average pressure acting on a circular surface corresponding to the active area of the sensors. In Fig. 9, a rather good agreement between the results of the two models (ZFM and MLM) and the experimental recording is observed. As discussed previously, the $C_p$ maximum values are not repeatable. To further illustrate this point, table 2 provides for each sensor the $C_p$ maximum values recorded for all tests. From these measurements, we computed the mean value of $C_p^{max}$ for each sensor. Interestingly, it appears that the mean values of $C_p^{max}$ are in fairly good agreement with the predictions of the Zhao-Faltinsen and Modified Logvinovitch models.

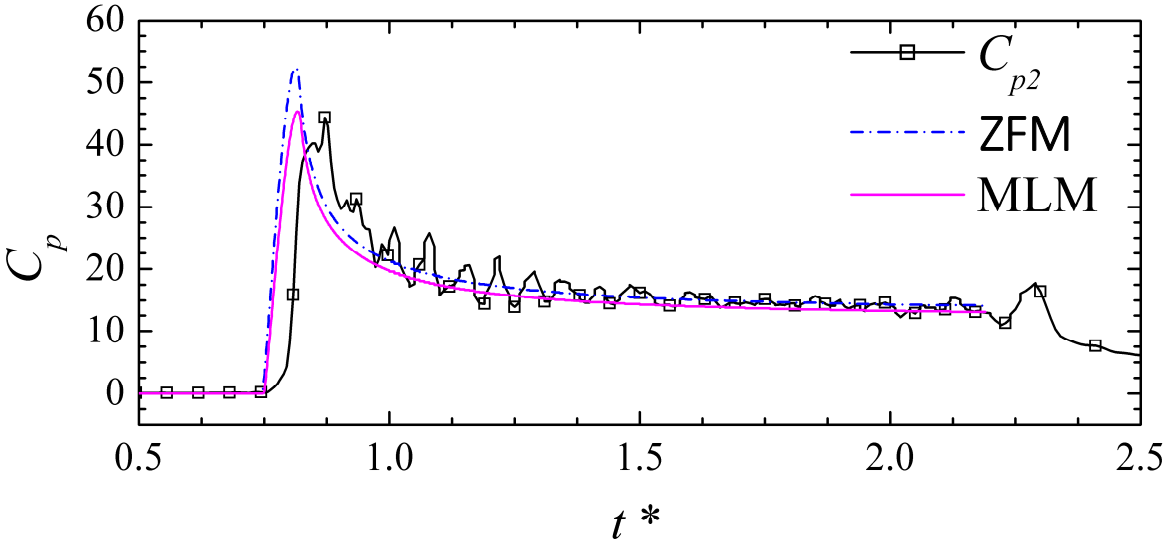


*Figure 9. Comparison between a pressure coefficient Cp profile from a test at $V_i$=9 m/s to theoretical profiles derived from the Zhao and Faltinsen model (ZFM) and the Modified Logvinovitch model (MLM).*

| Test | PCB2 | PCB3 | PCB4 | PCB5 |
|---|---|---|---|---|
| V5_T1 | 42.37 | 60.64 | 62.65 | 50.15 |
| V5_T2 | 46.57 | 38.05 | 61.95 | 60.05 |
| V5_T3 | 64.44 | 41.87 | 60.67 | 55.75 |
| V5_T4 | 52.59 | 48.73 | 68.12 | 62.63 |
| V7_T1 | 49.67 | 49.52 | 55.96 | 56.84 |
| V7_T2 | 32.94 | 46.12 | 63.31 | 52.46 |
| V7_T3 | 53.07 | 63.01 | 67.65 | 64.25 |
| V9_T1 | 45.04 | 49.36 | 63.40 | 53.17 |
| V9_T2 | 44.37 | 50.73 | 69.21 | 61.34 |
| V9_T3 | 50.49 | 62.40 | 60.86 | 63.27 |
| Mean experimental value | 48.16 | 51.04 | 63.38 | 57.99 |
| Relative standard deviation (%) | 16.2 | 15.8 | 6.03 | 8.2 |
| Zhao-Faltinsen model | 52.40 | 62.40 | 62.40 | 69.75 |
| MLM | 45.39 | 53.53 | 53.53 | 59.58 |

*Table 2. Maximum values of pressure coefficient $C_p^{max}$ recorderd at each sensor for all tests on pure water. The mean experimental value for each sensor and the standard deviation are also given, together with the predictions of the Zhao and Faltinsen model and the Modified Logvinovich model (obtained from the pressure averaged on the active area of the sensors).*

## 4.5 Pressure impulse

The pressure impulse is a quantity often used by coastal engineers in order to study the wave-impact-induced dynamic response of a structure. It is defined as the integral of the pressure between the impact start time $t_c$ and a time $t$ (after the impact):

$$\Pi(t) = \int_{t_c}^{t} p(t).d\tau \qquad (13)$$

The pressure impulse is relevant to the dynamic response of a structure, because it includes both peak and average pressure and impact duration. Moreover, being an integral of pressure over time, it is much less sensitive than the pressure maxima to the experimental conditions

such as the sampling frequency and the free surface shape [40]. Based on the pressure impulse, Cooker and Peregrine [8] derived a mathematical model describing the flow arising during the impact between a wave and a vertical wall.

We will use the pressure impulse to characterize the evolution of the loads on the cone during the impact. In order to compare pressure impulse results from various tests at different velocities, we will consider the dimensionless pressure impulse coefficient defined as:

$$I(t^*) = \int_{t_c^*}^{t^*} C_p(\tau^*).\mathrm{d}\tau^* \qquad (14)$$

In fact, the integral is taken between 0 and $t^*$, since the pressure is zero before $t_c^*$. For the specific case of a cone with a constant impact velocity, the Wagner theory provides a prediction of the evolution of the pressure impulse. Indeed, we derived the following expression of the pressure impulse coefficient as a function of $t^*$ (see appendix):

$$I(t^*) = C_p(\infty)\sqrt{t^{*2} - t_c^{*2}} \quad \text{for} \quad t^* > t_c^* \qquad (15)$$

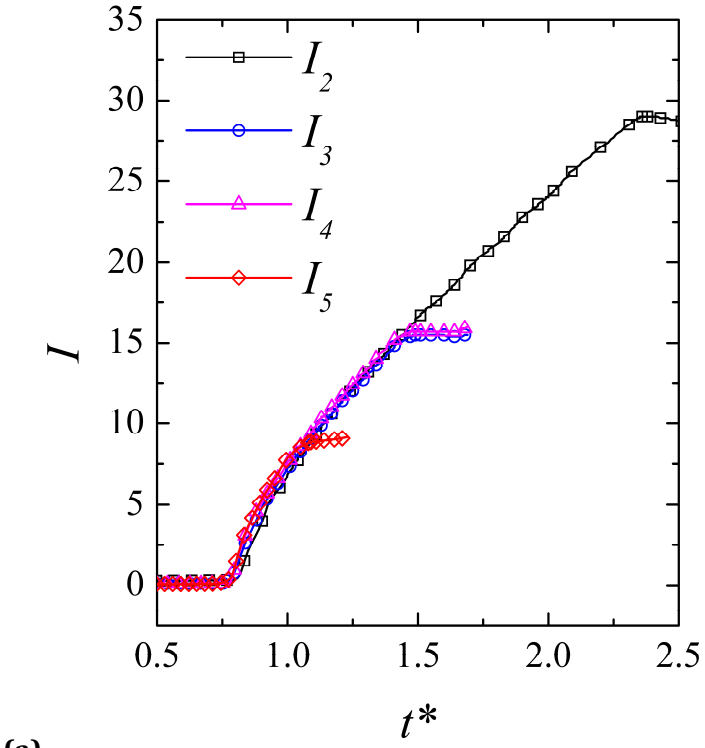


**(a)**

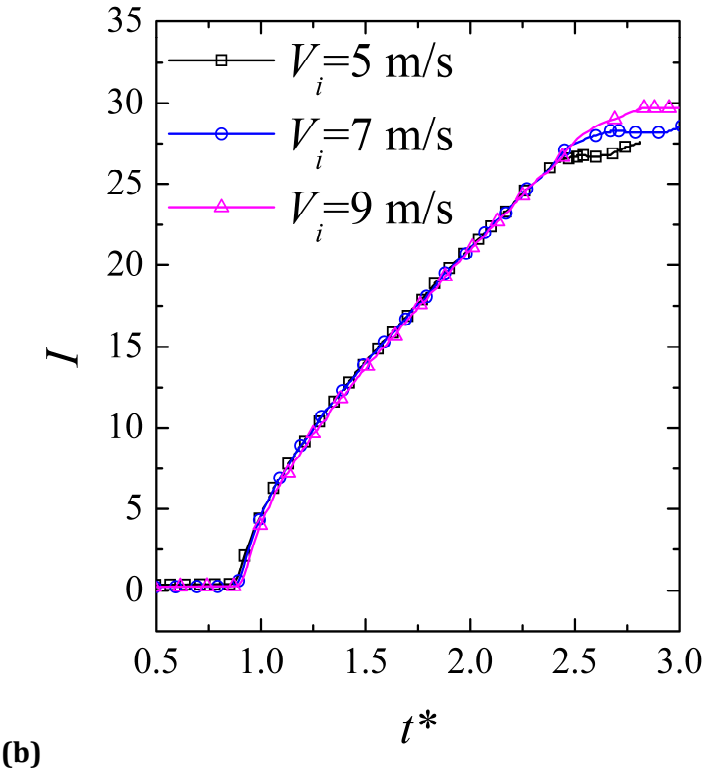


**(b)**

*Figure 10. Normalized pressure impulse coefficient I as a function of normalized time $t^*$. (a) Results obtained from all sensors for a test performed at $V_i$=9 m/s, (b) Results obtained from sensor PCB2 for several impact velocities.*

Fig. 10 shows that the rate of temporal growth of $I$ is indeed the same at the different positions and $I$ converges beyond the full immersion. Stated differently, Eq. (15) shows that $I^2$ varies linearly with $t^{*2}$ with a slope (linear coefficient) of $\mathrm{d}I^2/\mathrm{d}t^{*2} = C_p(\infty)^2$. Fig. 11 shows examples of the evolution of $I^2$ as a function of $t^{*2}$ obtained by integrating the pressure from the sensor PCB2, at which the longest recording before full immersion is found. The evolution of $I^2$ for all impact velocities is similar: it rises from zero a little after $t_c^*$ and increases until the time of the full immersion. After the full immersion[1], the pressure impulse reaches a nearly constant value as the impact pressure drops to values close to zero.

This linear relation can be verified from our results by applying a linear regression on the values of $I^2$ as a function of $t^{*2}$, as shown in Fig. 11. In all case, the coefficient of determination $R^2$ is larger than 99%. This shows that the linear regression reproduces very well the experimental evolution of $I^2$. This enables a straightforward comparison between experiments and Wagner theory results. Indeed, the linear regression yields an estimation of the coefficient $\left(\mathrm{d}I^2/\mathrm{d}t^{*2}\right)^{\frac{1}{2}}$ from the PCB2 signals. The values of this coefficient for all tests are given in table 3 and compared to the predictions of the Wagner model, the Zhao-Faltinsen model and the modified Logvinovitch model[2]. The experimental values are lying between 13.4 and 10.8, the maximum deviation being 20%. The scatter in the experimental data can be ascribed to various causes, including pressure fluctuations due to entrained air bubble oscillations and fluctuations in the entry velocities during the tests. The mean value of $\left(\mathrm{d}I^2/\mathrm{d}t^{*2}\right)^{\frac{1}{2}}$ concords well with the predictions of the analytical models, the best agreement being achieved with the modified Logvinovitch model.

[1] For the sensor PCB2, the Wagner theory predicts that full immersion occurs at $t^{*2} = 4.81$.

[2] With the ZFM and MLM, there is no closed-form expression for $\left(\mathrm{d}I^2/\mathrm{d}t^{*2}\right)^{1/2}$. The values given in table 3 have been obtained by numerical integration of the pressure signals.

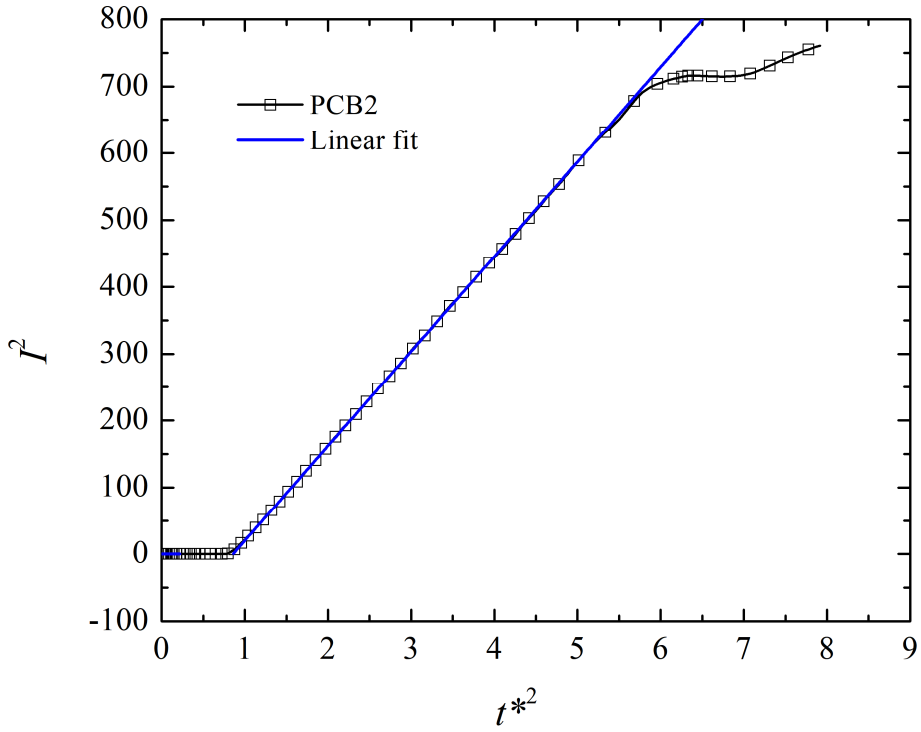


**(a)**

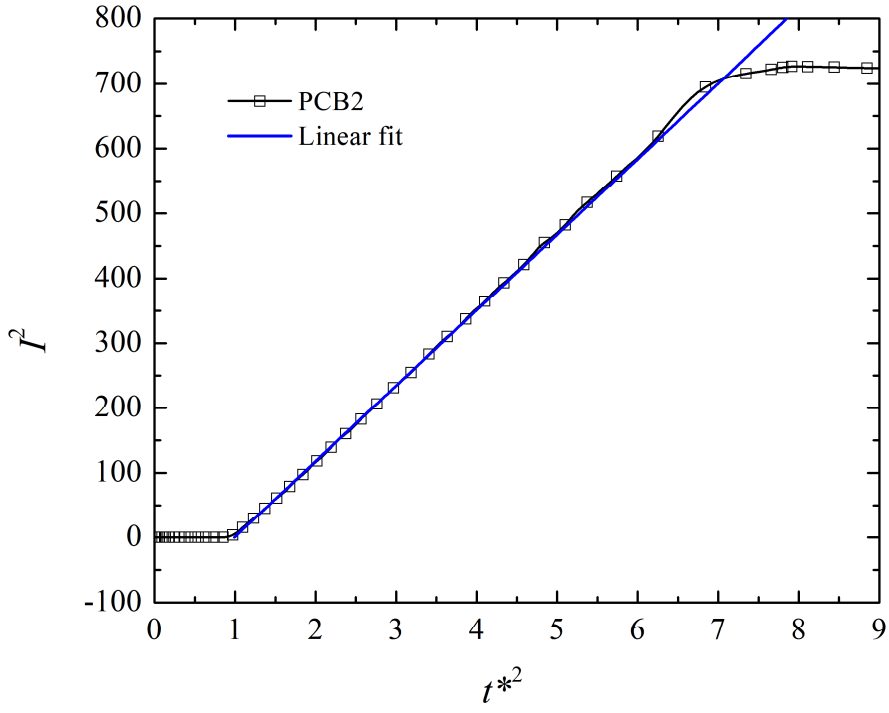


**(b)**

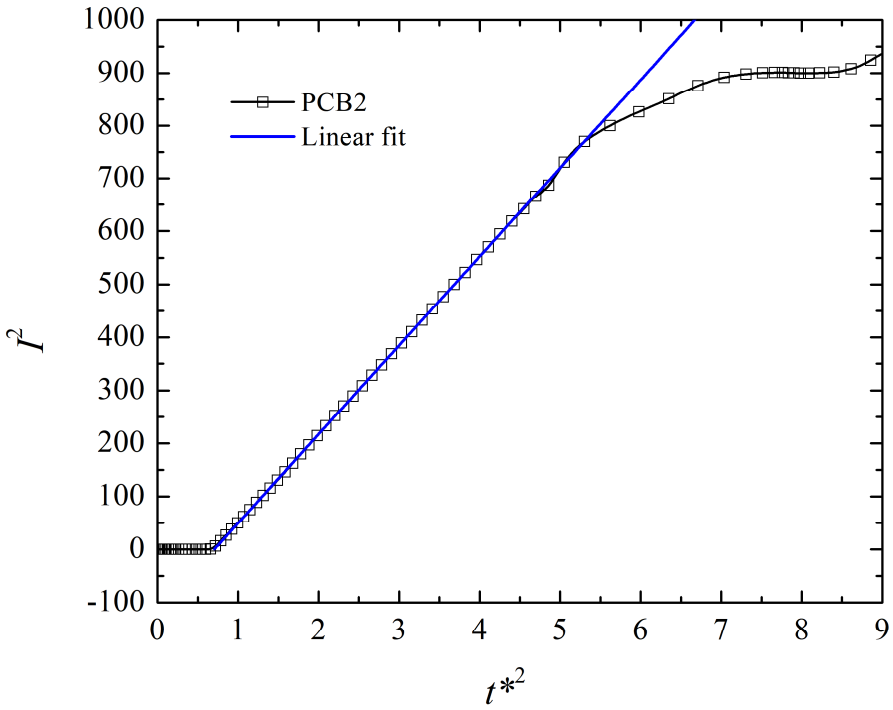


**(c)**

*Figure 11. Observation of the linear evolution of $I^2$ with $t^{*2}$ for impact tests on pure water at different impact velocities: (a) $V_i$=5 m/s, (b) $V_i$=7 m/s, (c) $V_i$=9 m/s.*

| Test | $\left(\mathrm{d}I^2/\mathrm{d}t^{*2}\right)^{\frac{1}{2}}$ |
|---|---|
| V5_T1 | 11.87 |
| V5_T2 | 12.15 |
| V5_T3 | 11.7 |
| V5_T4 | 13.4 |
| V7_T1 | 11.9 |
| V7_T2 | 10.8 |
| V7_T3 | 12.45 |
| V9_T1 | 11.9 |
| V9_T2 | 12.60 |
| V9_T3 | 12.95 |
| Mean experimental value | 12.2 |
| Relative standard deviation (%) | 5.9 |
| Wagner model | 13.2 |
| Zhao-Faltinsen model | 12.9 |
| MLM | 11.8 |

*Table 3. Values of the coefficient* $\left(\mathrm{d}I^2/\mathrm{d}t^{*2}\right)^{\frac{1}{2}}$ *obtained for all tests from the pressure signals recorded at the sensor PCB2. The mean experimental value and the standard deviation are also given, together with the predictions of the Wagner, Zhao-Faltinsen and modified Logvinovich models.*

# 5 Effect of aeration

In addition to the impacts on pure water, we performed impact tests on aerated water in order to investigate how the aeration affects the pressure distribution on the cone surface during the impact. The aeration set-up and void fraction measurements are described in section 3. In the present experiments, we considered two values of the average void fraction, $\alpha_0 = 0.35\%$ and 1.10%, and two impact velocities, $V_i = 5$ m/s and 9 m/s. For each experimental condition, at least four tests were performed. The corresponding instantaneous pressure, as well as the pressure impulse are hereafter presented and discussed.

## 5.1 Instantaneous pressure

Fig. 12 shows impact test results in terms of typical pressure signals from all sensors for several values of void fraction, $\alpha_0 = 0\%$, 0.35% and 1.10% and two impact velocities, $V_i = 5$ m/s and 9 m/s. In many aspects, the evolution of the impact pressure with time is similar to that for $\alpha_0 = 0$. The pressure first increases when the sensor touches the free surface, then it decreases relatively slowly. However, the pressure is generally smaller for $\alpha_0 > 0$. At $V_i = 5\ m/s$, most of the pressure maxima are larger and smaller than 7 bars for $\alpha_0$=0% and 1.1%, respectively. Also, the commencements of the rise in pressure signals from the PCB3 and PCB4 are no longer simultaneous when $\alpha_0 > 0$. Moreover, the shifts between the two signals become larger with increasing void fraction $\alpha_0$. This suggests that the expansion velocity varies with the radial position in the case of an impact on aerated water, indicating that the axis-symmetry of the flow deteriorates.

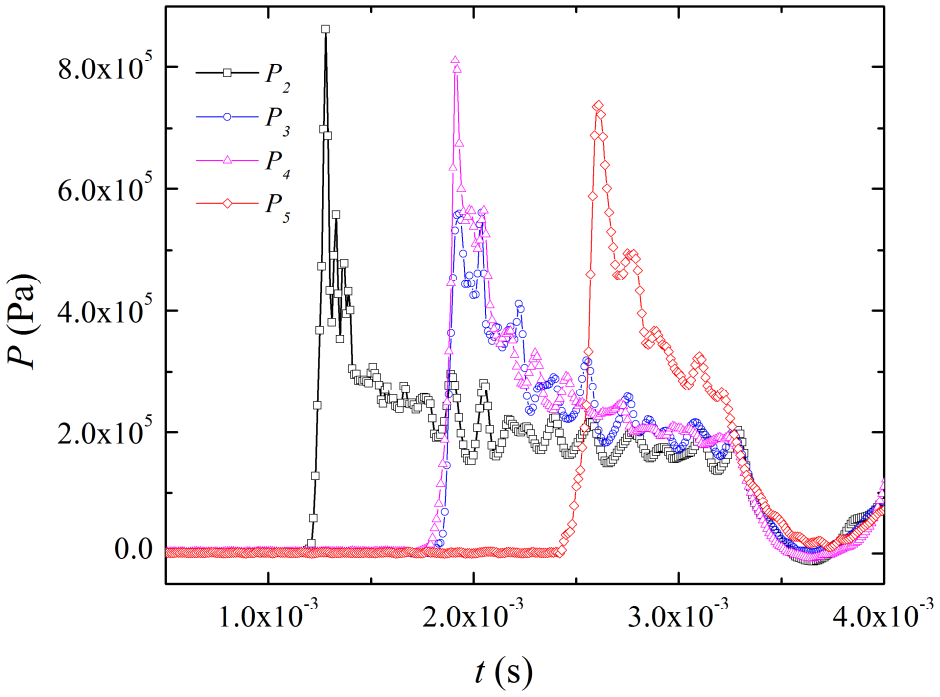


**(a)**

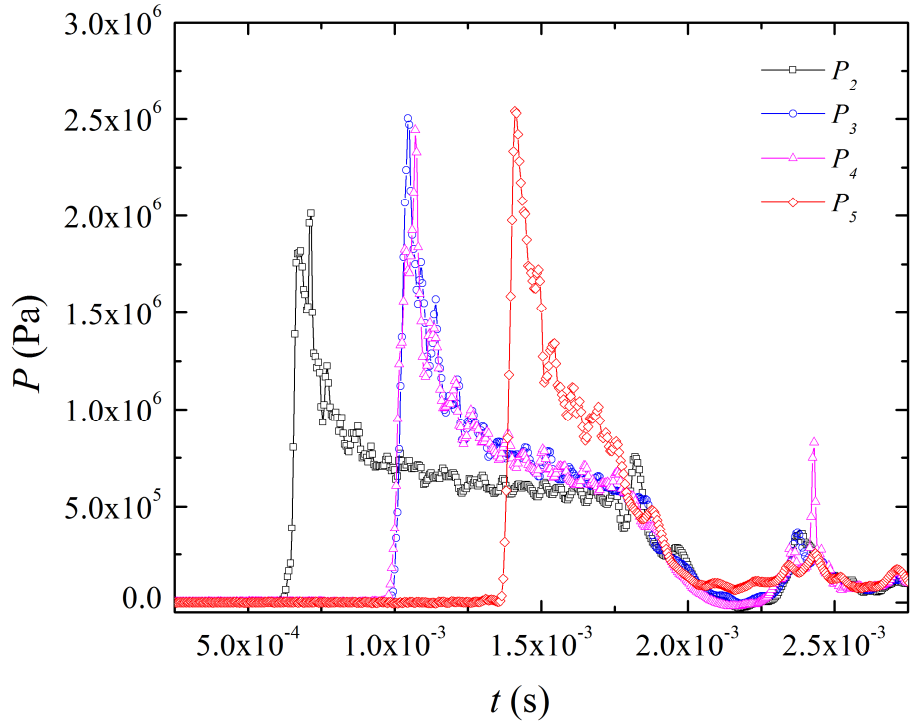
3.0x10^6
2.5x10^6
2.0x10^6
1.5x10^6
1.0x10^6
5.0x10^5
0.0
P (Pa)
5.0x10^-4
1.0x10^-3
1.5x10^-3
2.0x10^-3
2.5x10^-3
t (s)
P2
P3
P4
P5

**(b)**

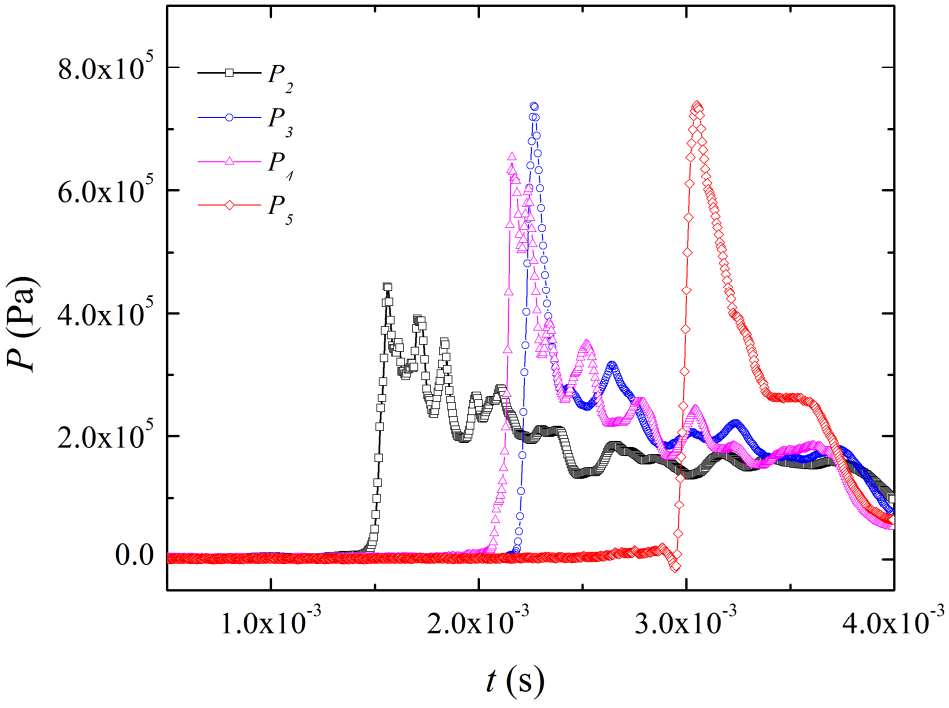
8.0x10^5
6.0x10^5
4.0x10^5
2.0x10^5
0.0
P (Pa)
1.0x10^-3
2.0x10^-3
3.0x10^-3
4.0x10^-3
t (s)
P2
P3
P1
P5

**(c)**

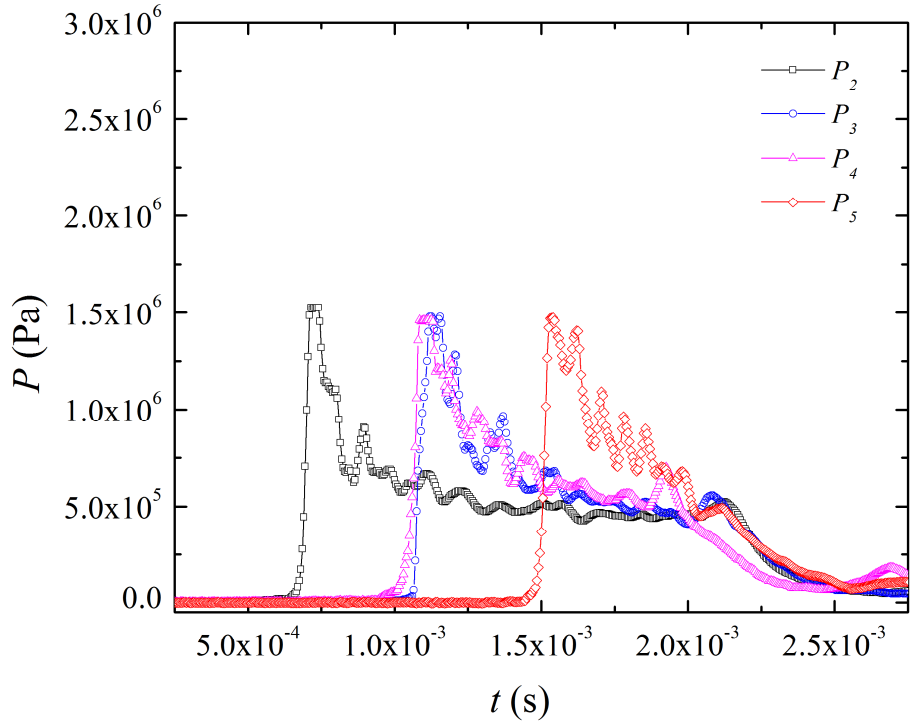
3.0x10^6
2.5x10^6
2.0x10^6
1.5x10^6
1.0x10^6
5.0x10^5
0.0
P (Pa)
5.0x10^-4
1.0x10^-3
1.5x10^-3
2.0x10^-3
2.5x10^-3
t (s)
P2
P3
P4
P5

**(d)**

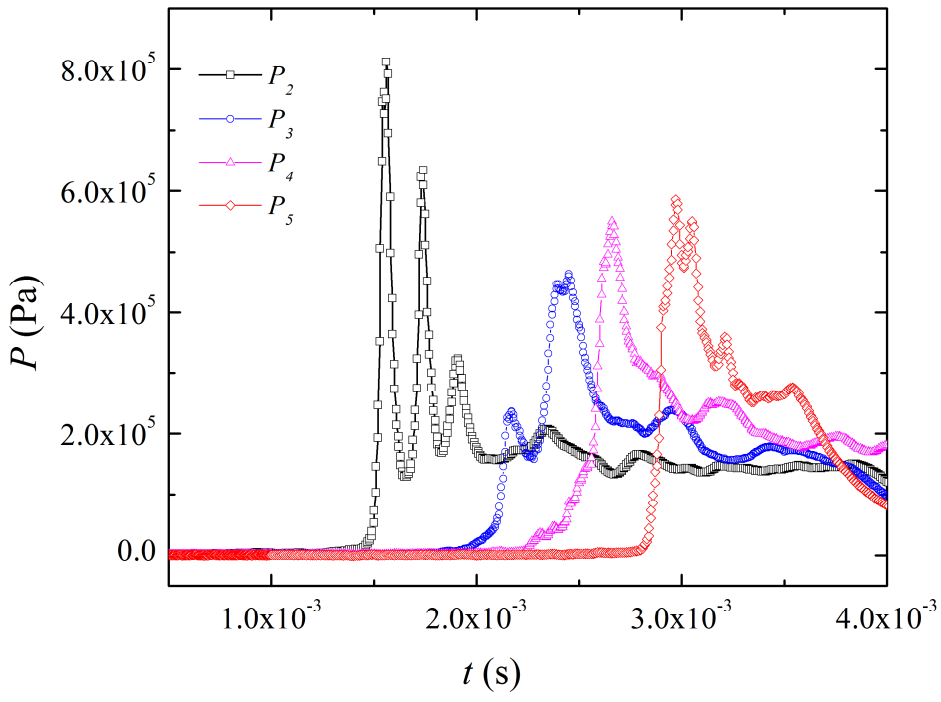
8.0x10^5
6.0x10^5
4.0x10^5
2.0x10^5
0.0
P (Pa)
1.0x10^-3
2.0x10^-3
3.0x10^-3
4.0x10^-3
t (s)
P2
P3
P4
P5

**(e)**

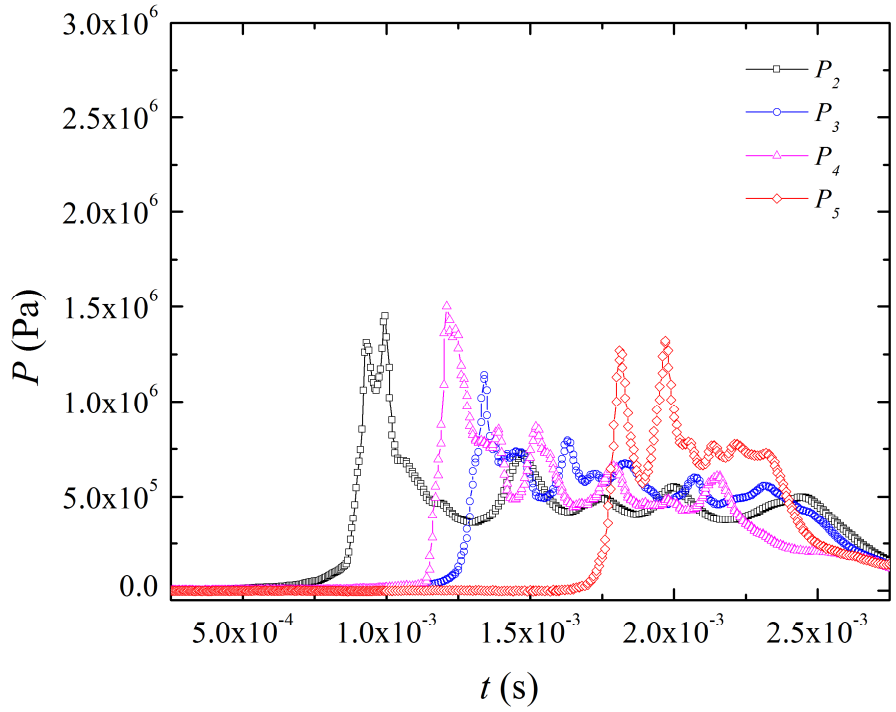


**(f)**

*Figure 12. Examples of instantaneous pressure signals from the four pressure sensors at two different impact velocities,* (a) $V_i$= 5m/s; $\alpha_0$=0%, (b) $V_i$= 9m/s; $\alpha_0$=0%, (c) $V_i$= 5m/s; $\alpha_0$=0.35%, (d) $V_i$= 9m/s; $\alpha_0$=0.35%, (e) $V_i$= 5m/s; $\alpha_0$=1.10% and (f) $V_i$= 9m/s; $\alpha_0$=1.10%.

The values of the expansion velocity estimates, $V_{32}$ and $V_{53}$ (see Eq. (10)), were calculated using the same method as in the previous section. No clear trend was observed with aeration, since no significant increase or decrease could be inferred from our results, as there is a great variability of the time of first contact with water at a given position on the cone.

Pressure coefficient evolutions obtained for $\alpha_0 = 0.35\%$ and $\alpha_0 = 0.35\%$ and different impact velocities are shown in Fig. 13. For $\alpha_0 = 0$ (see Fig. 7), these curves were very close to each other, as a result of the self-similarity of the flow. For all cases where $\alpha_0 > 0$, significant discrepancies are observed between the values of the $C_p$ from the four sensors. This clearly evidences a departure from self-similarity of the instantaneous flow around the cone, due to the aeration. This departure from self-similarity is enhanced when increasing the void fraction ($\alpha_0$=1.1%) and is closely linked to a shift in $t_c^*$ at different given positions on the cone. Most probably, this is a consequence of the spatially uneven distribution of the bubbles in the bubble plume (or in other words the heterogeneity of the void volume fraction distribution), which changes locally the shape of the contact surface at a given instant. Table 4 provides the average maximum pressure coefficient $C_p^{max}$ for several initial void fractions $\alpha_0$ and impact velocities $V_i$.

For each experimental condition (characterized by $\alpha_0$ and $V_i$), the average value of $C_p^{max}$ has been calculated by considering the records of the four sensors and all the tests carried out. It clearly appears that the average maximum pressure coefficient decreases with the initial void fraction. For both impact velocities, the value of $C_p^{max}$ for $\alpha_0$ =1.1 % is about 25 % smaller than that for pure water ($\alpha_0 = 0$). It is interesting to mention that Elhimer et al. [31] observed that for the same cone geometry and void fraction of 1.1% a global hydrodynamic force reduction of 30 % (in comparison with pure water). This means that the peak pressure reduction is lesser than the force reduction. A possible reason of this phenomenon is that the force reduction is not only due to a decrease in the pressure acting on the wetted surface but also to a change of the (average) expansion velocity of the wetted surface.

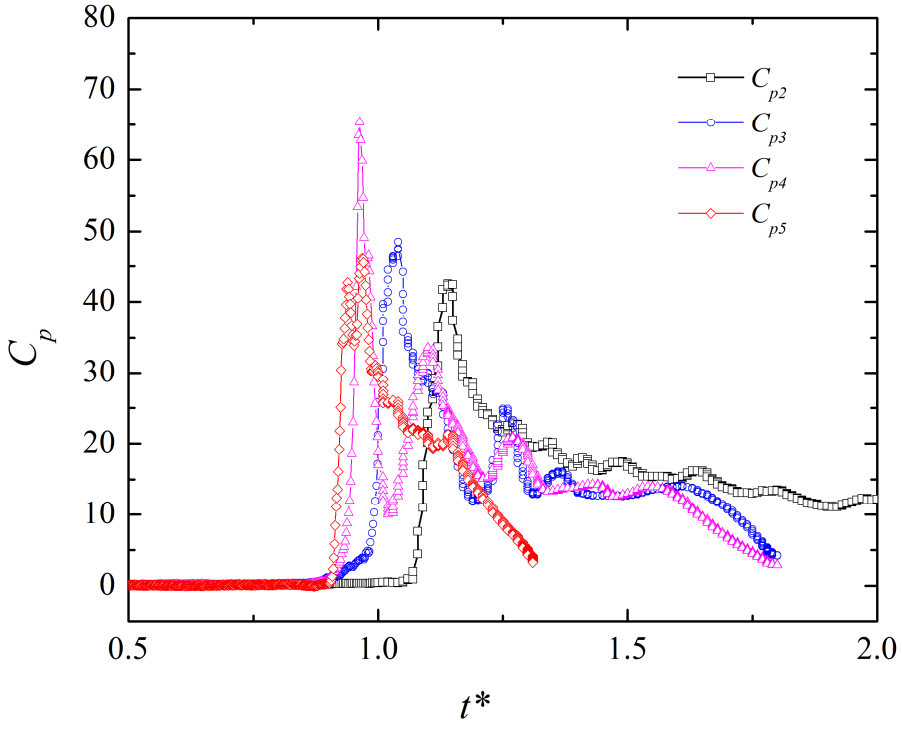


**(a)**

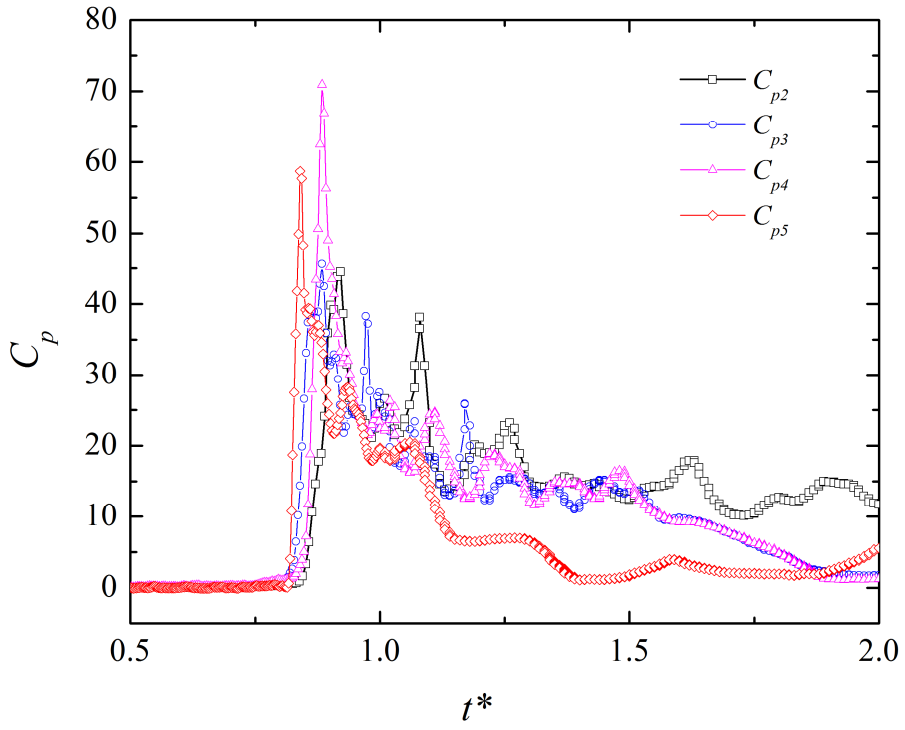
80
70
60
50
40
30
20
10
0
0.5
1.0
1.5
2.0
$C_p$
$t^*$
$C_{p2}$
$C_{p3}$
$C_{p4}$
$C_{p5}$

**(b)**

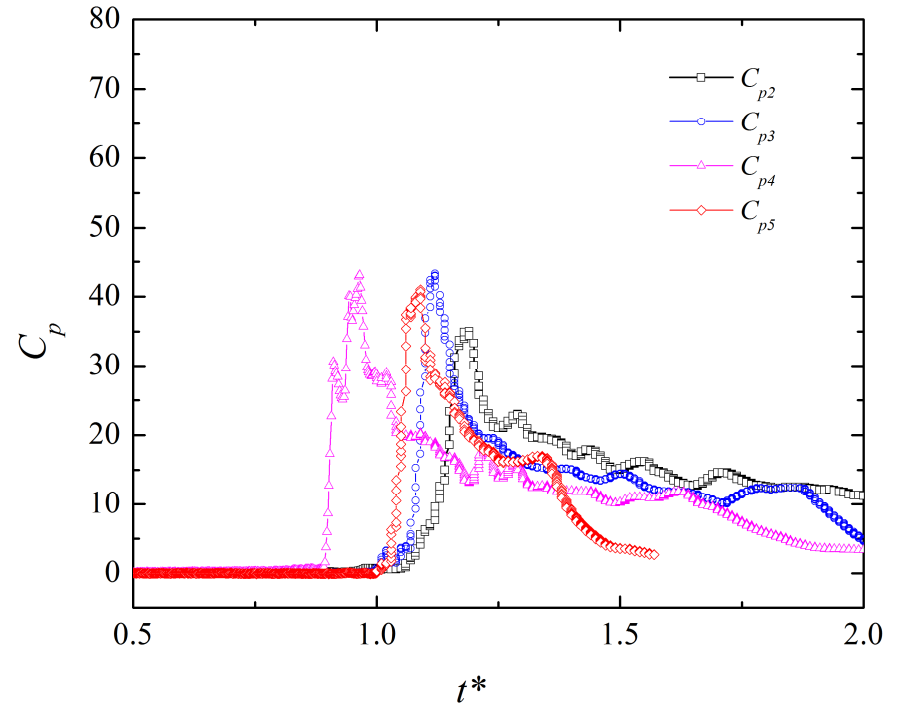
80
70
60
50
40
30
20
10
0
0.5
1.0
1.5
2.0
$C_p$
$t^*$
$C_{p2}$
$C_{p3}$
$C_{p4}$
$C_{p5}$

**(c)**

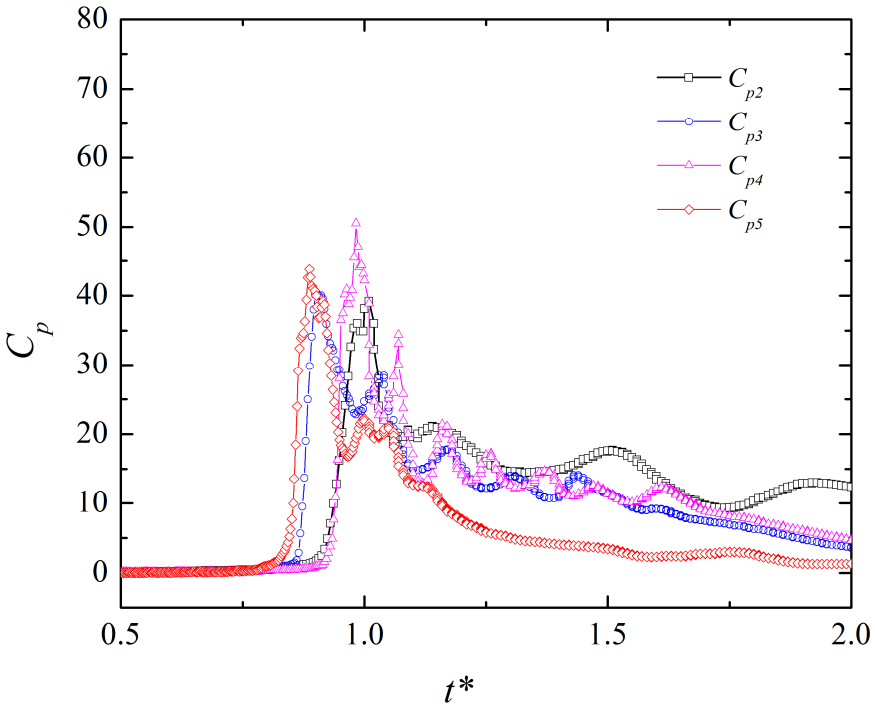


**(d)**

*Figure 13. Examples of the evolution of the pressure coefficient $C_p$ with normalized time t* from the four sensors at two different impact velocities,*
(a) $V_i$= 5m/s; $\alpha_0$=0.35%, (b) $V_i$= 9m/s; $\alpha_0$=0.35%, (c) $V_i$= 5m/s; $\alpha_0$=1.10% and (d) $V_i$= 9m/s; $\alpha_0$=1.10%.

| $\alpha_0$ (%) | $V_i$ (m/s) | $C_p^{max}$ average value | Relative standard deviation (%) |
|---|---|---|---|
| 0 | 5 | 54.8 | 16.3 |
| | 9 | 56.1 | 14 |
| 0.35 | 5 | 47.5 | 18.2 |
| | 9 | 45.6 | 25.1 |
| 1.1 | 5 | 42.9 | 23 |
| | 9 | 38.4 | 15.1 |

*Table 4. Experimental average values and relative standard deviations for the maximum pressure coefficient $C_p^{max}$ obtained for several void volume fraction $\alpha_0$ and impact velocity $V_i$. For each experimental condition ($\alpha_0$, $V_i$), the records of the four sensors and all the tests carried out have been considered.*

## 5.2 Pressure impulse

In the case of pure water, the scaling of the pressure impulse with time is well predicted by a linear model derived from the Wagner theory. We also examined the evolution of the pressure impulse with aerated water. Examples of normalized pressure impulse coefficient evolutions (from sensor PCB2) for two values of $V_i$ and $\alpha_0$ are shown in Fig. 14. For all the tests, the evolution of $I^2$ with respect to $t^{*2}$ is similar to the case of pure water. $I^2$ still scales linearly with $t^{*2}$ (before flow separation at the cone knuckle) in the case of aerated water.

We have therefore applied the linear regression analysis described in section 4.5 to determine the coefficient $\left(\mathrm{d}I^2/\mathrm{d}t^{*2}\right)^{1/2}$ for each test on aerated water (using PCB2 signal). The results are presented in Fig. 15, that displays the evolution of $\left(\mathrm{d}I^2/\mathrm{d}t^{*2}\right)^{1/2}$ with the initial void fraction for two impact velocities, $V_i$ =5 m/s and 9 m/s. The value of $\left(\mathrm{d}I^2/\mathrm{d}t^{*2}\right)^{1/2}$ associated to the Wagner theory (in which the fluid is assumed incompressible) is also shown in Fig. 15. First, it is interesting to observe that the measurements of the coefficient $\left(\mathrm{d}I^2/\mathrm{d}t^{*2}\right)^{1/2}$ are quite reproducible. The scatter of the experimental data for aerated water is not significantly greater than for pure water. The results highlight a clear decrease in $\left(\mathrm{d}I^2/\mathrm{d}t^{*2}\right)^{1/2}$with increasing void fraction, showing that the rate of increase of the pressure impulse diminishes due to the aeration. Note also that the values of $\left(\mathrm{d}I^2/\mathrm{d}t^{*2}\right)^{1/2}$ for aerated liquids ($\alpha_0$ =0.35 % and 1.1 %) are significantly lower than the prediction of the Wagner theory. This suggests that the pressure impulse reduction due to aeration is related to the enhanced compressibility of the air-water mixture. This finding confirms the results of the numerical simulations presented in Ma et al.[29] and Elhimer et al.[31]. The average value of $\left(\mathrm{d}I^2/\mathrm{d}t^{*2}\right)^{1/2}$ for $\alpha_0$ =1.1 % is about 20% smaller than for pure water. This decrease is close to that of the maximum pressure coefficient (see section 5.1). This suggests that aeration causes a similar pressure reduction over the entire wetted surface.

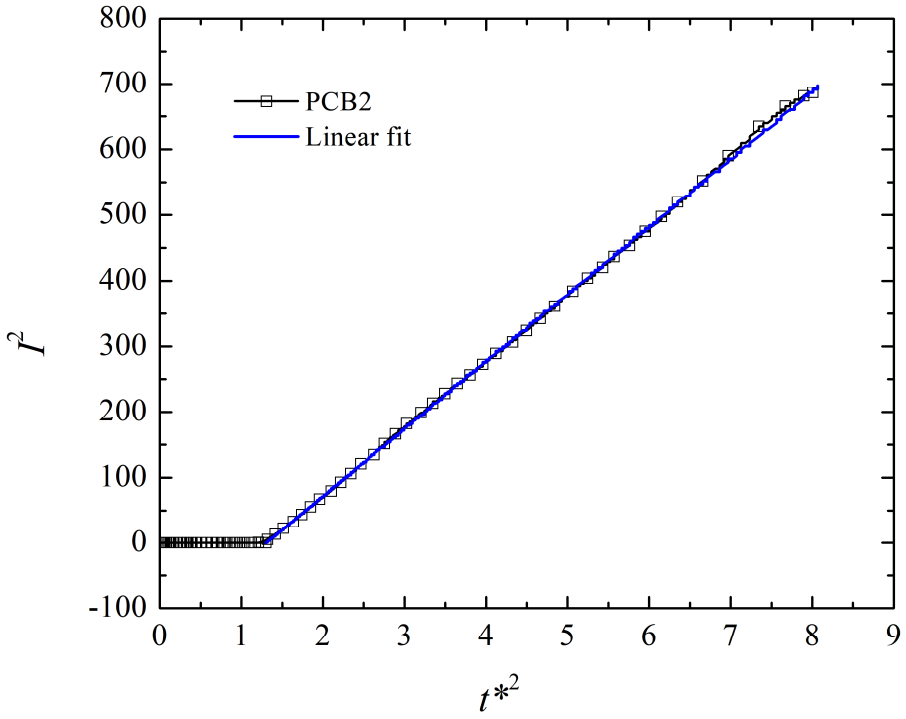


**(a)**

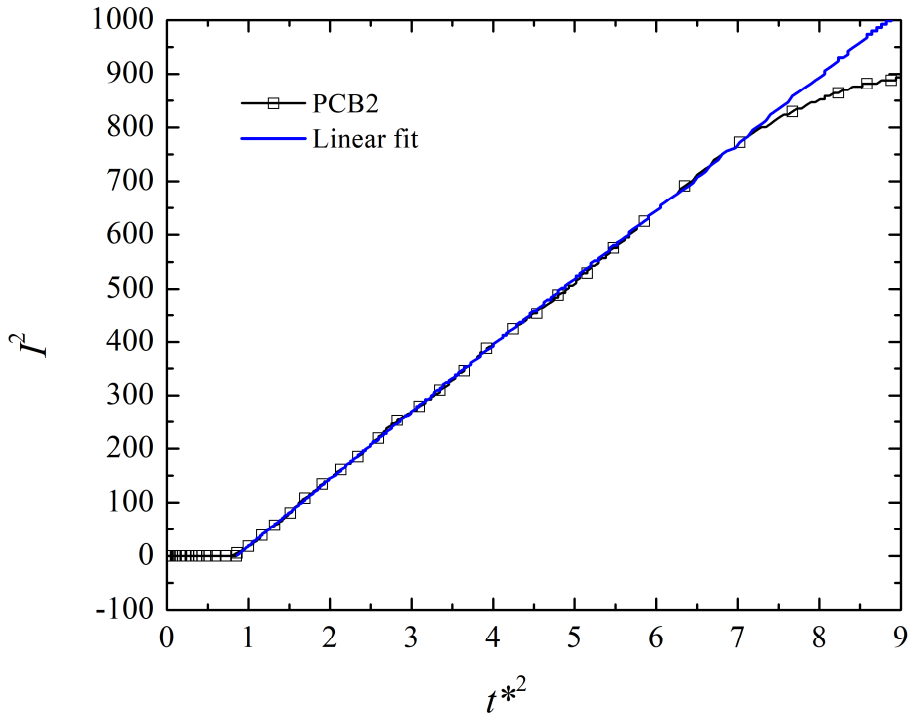


**(b)**

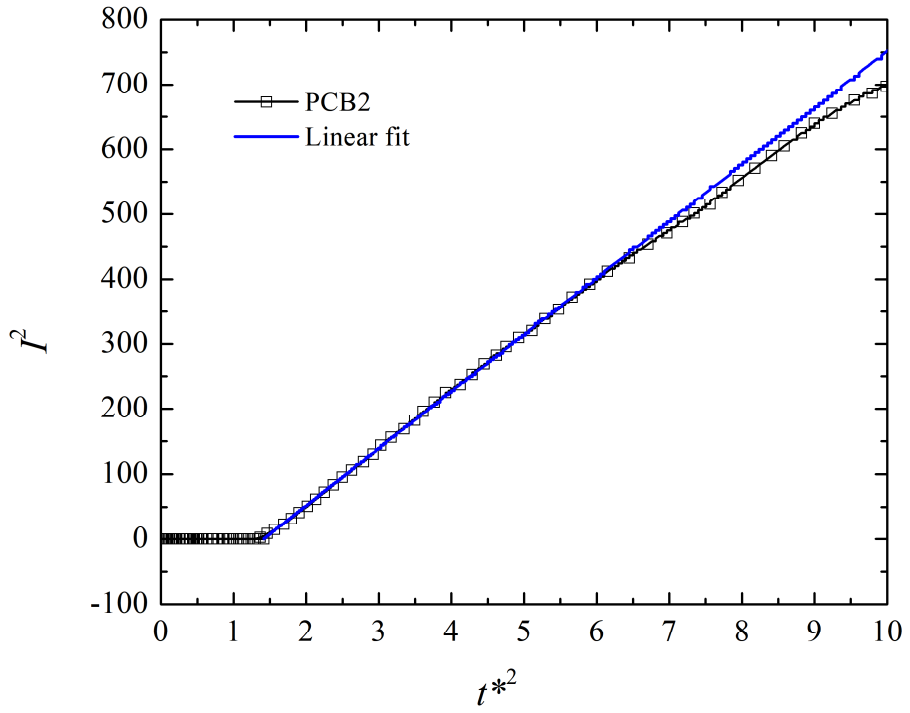


**(c)**

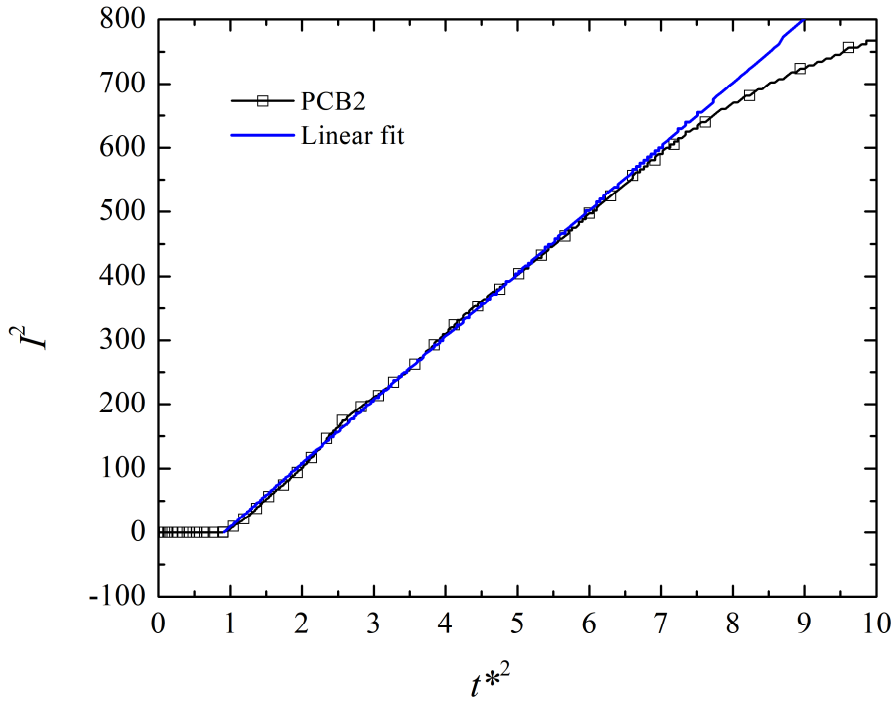


**(d)**

*Figure 14. Examples of evolutions of the squared pressure impulse coefficient $I^2$ with normalized time t* for impact tests on aerated water for several impact velocities $V_i$ and initial void fraction $\alpha_0$.* (a) $V_i$= 5m/s; $\alpha_0$=0.35%, (b) $V_i$= 9m/s; $\alpha_0$=0.35%, (c) $V_i$= 5m/s; $\alpha_0$=1.10% and (d) $V_i$= 9m/s; $\alpha_0$=1.10%. *Straight lines correspond to a linear fit of the experimental results.*

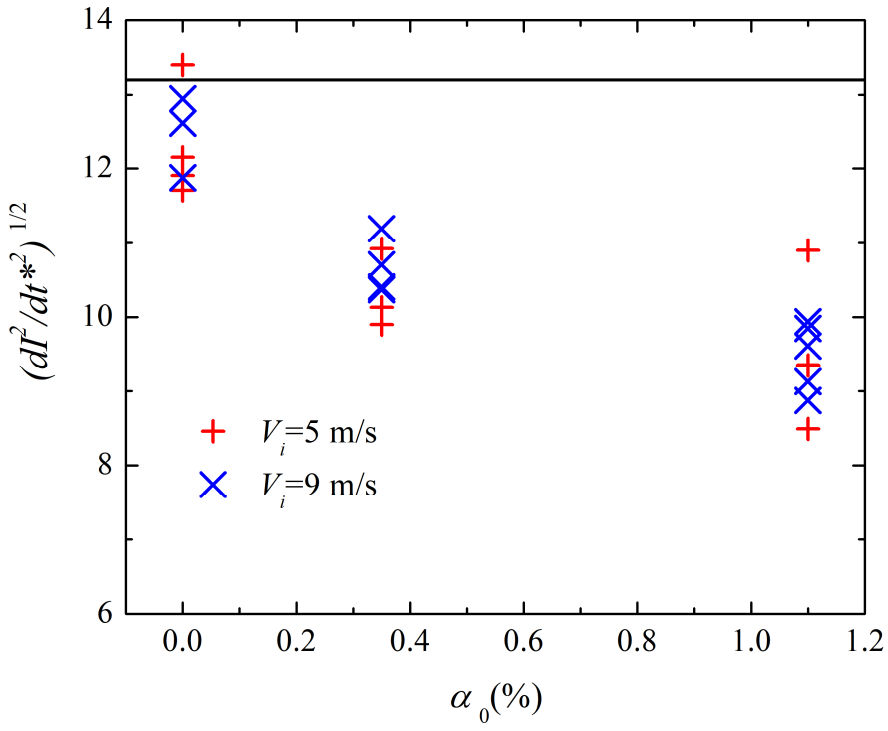


*Figure 15. Evolution of the coefficient* $\left(\mathrm{d}I^2/\mathrm{d}t^{*2}\right)^{1/2}$ *from sensor PCB2 with the initial mean void volume fraction* $\alpha_0$ *for two impact velocities,* $V_i$ *=5 m/s and 9 m/s. The straight line corresponds to the theoretical value from Wagner's theory.*

# 6 Conclusions

In this study, we investigated the influence of impact velocity and aeration on the time evolution of the impact pressure during cone water entry. We conducted impact tests on a rigid cone with a small deadrise angle ($\beta$=7°) at constant impact velocities using a shock testing hydraulic machine. Three values of the impact velocity, $V_i = 5,\ 7$ and 9 m/s, and three values of the mean void fraction, $\alpha_0 = 0\%, 0.35\ \%$ and $1.1\ \%$, were considered in the impact tests. The instantaneous impact pressure was measured at four different locations on the cone surface. The experimental results were also analyzed using the pressure impulse. From an experimental point of view, the pressure impulse is confirmed to be less prone to large fluctuations while retaining the physics of the evolution of the impact pressure.

A simple analytical model for the evolution of the pressure and pressure impulse coefficients, based on the Wagner theory and its extensions, was assessed. In the case of pure water impacts, the Wagner theory is found to provide good prediction of the scaling of the wetted surface

expansion velocity $V_c$ with the impact velocity $V_i$. The pressure and pressure impulse distributions are also well described by the Wagner theory.

Aeration is shown to induce a significant reduction of the impact pressure. A decrease of about 25 % (in comparison to the pure water case), for both the peak pressures and the rate of increase of the pressure impulse, was observed for a void volume fraction of 1.1 %. An interesting observation is that, in presence of aeration, the pressure distribution is no longer axisymmetric and self-similar. This phenomenon is probably due to inhomogeneous distributions of the bubbles in the water and free-surface disturbances caused by the bubble-rising motions. The influence of void-fraction inhomogeneities and bubble motions certainly deserves to be further investigated in future works. Using a generator producing smaller bubbles (using for instance a sintered metal plate with small pores) should lead to a more homogeneous void fraction distribution and limit bubble-induced disturbances. Moreover, the use of a surfactant can reduce the bubble rising velocity [41].

## Acknowledgments

The authors would like to thank all technicians of ENSTA Bretagne for their help in experimental set-up. This work is part of a research program supported by DGA (French Armaments Procurement Agency). The financial support by DGA (Grant n° 2012.60.0010.00.470.75.01) was also greatly appreciated.

## Data availability

The data that support the findings of this study are available from the corresponding author upon reasonable request.

## Appendix: Derivation of the expression of the pressure impulse coefficient with the Wagner model

The Wagner model (see Eq. (5)) yields the following expression of the pressure coefficient:

$$C_p(\tau^*) = \frac{4}{\pi}\frac{V_c}{Vi}\left(1 - \frac{t_c^{*2}}{\tau^{*2}}\right)^{-1/2}$$

To compute the dimensionless pressure impulse coefficient, Eq. (14), we use the integration by substitution method to find the integral of $C_p(\tau^*)$ between $t_c^*$ and a subsequent normalized time $t^*$. Let us substitute the normalized $\tau^*$ with a new variable $T$ defined as $T = t_c^*/\tau^*$ in the expression of $C_p$ :

$$C_p = C_p(\infty)(1-T^2)^{-\frac{1}{2}} \qquad \text{with} \qquad C_p(\infty) = \frac{4}{\pi}\frac{V_c}{Vi}$$

Considering that $\mathrm{d}\tau^* = -t_c^* T^{-2}\mathrm{d}T$, $\tau^* = t_c^* \rightarrow \ T = 1$ and $\tau^* = t^* \rightarrow \ T = \frac{t_c^*}{t^*}$, the integration by substitution leads to :

$$I(t^*) = \int_{t_c^*}^{t^*} C_p(\tau^*)\mathrm{d}\tau^* = C_p(\infty)\int_{\frac{t_c^*}{t^*}}^{1} \frac{t_c^*}{T^2\sqrt{1-T^2}}\mathrm{d}T$$

Therefore, the following expression of the dimensionless pressure impulse coefficient is obtained:

$$I(t^*) = C_p(\infty)t_c^*\left[-\frac{\sqrt{1-T^2}}{T}\right]_{\frac{t_c^*}{t^*}}^{1} = C_p(\infty)\sqrt{t^{*2}-t_c^{*2}}$$

# References


1. Oumeraci, H. Review and analysis of vertical breakwater failures lessons learned. *Coast. Eng.* 3–29 (1994).

2. Dias, F. & Ghidaglia, J. Slamming : Recent Progress in the Evaluation of Impact Pressures. *Annu. Rev. Fluid Mech.* 243–273 (2018).

3. Lafeber, W., Brosset, L. & Bogaert, H. Comparison of wave impact tests at large and full scale: Results from the sloshel project. *Proc. Int. Offshore Polar Eng. Conf.* 285–299 (2012).

4. Von Karman, T. Von. *The impact on seaplane floats during landing*. (1929).

5. Wagner, H. Über Stoß- und Gleitvorgänge an der Oberfläche von Flüssigkeiten. *J. Appl. Math. Mech. / Zeitschrift für Angew. Math. und Mech.* **12**, 193–215 (1932).

6. Zhao, Z. R. & Faltinsen, F. O. Water entry of two-dimensional bodies. *J. Fluid Mech.* **246**, 593–612 (1993).

7. Korobkin, A. Analytical models of water impact. *Eur. J. Appl. Math.* **15**, 821–838 (2004).

8. Cooker, M. J. & Peregrine, D. H. Pressure-impulse theory for liquid impact problems. *J.*

*Fluid Mech.* **297**, 193–214 (1995).

9. Peregrine, D. H. Water-wave impact on walls. *Annu. Rev. Fluid Mech.* **35**, 23–43 (2003).

10. Frandsen, J. B. & Bérubé, F. Large scale experimental wave impact on walls in the Québec Coastal Physics Laboratory. *Proc. Int. Conf. Offshore Mech. Arct. Eng. - OMAE* **7**, (2015).

11. El Malki Alaoui, A., Nême, A., Tassin, A. & Jacques, N. Experimental study of coefficients during vertical water entry of axisymmetric rigid shapes at constant speeds. *Appl. Ocean Res.* **37**, 183–197 (2012).

12. Peseux, B., Gornet, L. & Donguy, B. Hydrodynamic impact: Numerical and experimental investigations. *J. Fluids Struct.* **21**, 277–303 (2005).

13. Tassin, A., Jacques, N., El Malki Alaoui, A., Nême, A. & Leblé, B. Assessment and comparison of several analytical models of water impact. *Int. J. Multiphys.* **4**, 125–140 (2010).

14. Tassin, A., Jacques, N., El Malki Alaoui, A., Nême, A. & Leblé, B. Hydrodynamic loads during water impact of three-dimensional solids: Modelling and experiments. *J. Fluids Struct.* **28**, 211–231 (2012).

15. Bullock, G. ., Crawford, A. ., Hewson, P. ., Walkden, M. J. . & Bird, P. A. . The influence of air and scale on wave impact pressures. *Coast. Eng.* **42**, 291–312 (2001).

16. Bullock, G. N., Obhrai, C., Peregrine, D. H. & Bredmose, H. Violent breaking wave impacts. Part 1: Results from large-scale regular wave tests on vertical and sloping walls. *Coast. Eng.* **54**, 602–617 (2007).

17. Bredmose, H., Peregrine, D. H. & Bullock, G. N. Violent breaking wave impacts. Part 2: modelling the effect of air. *J. Fluid Mech.* **641**, 389–430 (2009).

18. Hattori, M., Arami, A. & Yui, T. Wave impact pressure on vertical walls under breaking waves of various types. *Coast. Eng.* **22**, 79–114 (1994).

19. Walkden, A. Model wave impulse loads on caisson breakwaters: aeration, scale and structural response. (University of Plymouth, 1999).

20. Chuang, W.-L., Chang, K.-A. & Mercier, R. Impact pressure and void fraction due to plunging breaking wave impact on a 2D TLP structure. *Exp. Fluids* **58**, 68 (2017).

21. Brennen, C. E. *Fundamentals of Multiphase Flows*. vol. 128 (Cambridge University Press, 2005).

22. Bullock, G. N., Crawford, A. R., Hewson, P. J., Walkden, M. J. A. & Bird, P. A. D. The influence of air and scale on wave impact pressures. *Coast. Eng.* 291–312 (2001).

23. Ceccio, S. L. Friction Drag Reduction of External Flows with Bubble and Gas Injection. *Annu. Rev. ofFluid Mech.* **42**, 183–203 (2010).

24. Murai, Y. Frictional drag reduction by bubble injection. *Exp. Fluids* **55**, 1773 (2014).

25. Young, Y. L., Harwood, C. M., Miguel Montero, F., Ward, J. C. & Ceccio, S. L. Ventilation of Lifting Bodies: Review of the Physics and Discussion of Scaling Effects. *Appl. Mech. Rev.* **69**, (2017).

26. Eroshin, V. A., Romanenkov, N. I., Serebryakov, I. V. & Yakimov, Y. L. Hydrodynamic forces produced when blunt bodies strike the surface of a compressible fluide. *Fluid Dyn.* **15**, 829–835 (1980).

27. Eroshin, V. A., Plyusnin, A. V., Romanenkov, N. I., Sozonenko, Y. A. & Yakimov, Y. L. Influence of the atmosphere on the magnitude of the hydrodynamic forces in the case of a disk in a flat encounter with the surface of a compressible liquid. *Fluid Dyn.* **19**, (1984).

28. Eroshin, V. A., Konstantinov, G. A., Romanenkov, N. I. & Yakimov, Y. L. Experimental determination of the pressure on a disk entering a compressible fluid at an angle to the free surface. *Fluid Dyn.* **23**, (1988).

29. Ma, Z. H. *et al.* Pure and aerated water entry of a flat plate. *Phys. Fluids* **28**, 016104 (2016).

30. Mai, T., Mai, C., Raby, A. & Greaves, D. M. Aeration effects on water-structure impacts: Part 1. drop plate impacts. *Ocean Eng.* **193**, 106600 (2019).

31. Elhimer, M., Jacques, N., El Malki Alaoui, A. & Gabillet, C. The influence of aeration and compressibility on slamming loads during cone water entry. *J. Fluids Struct.* **70**, 24–46 (2017).

32. El Malki Alaoui, a., Nême, a. & Scolan, Y. M. Experimental investigation of hydrodynamic loads and pressure distribution during a pyramid water entry. *J. Fluids Struct.* **54**, 925–935 (2015).

33. Korobkin, A. A. & Scolan, Y. M. Three-dimensional theory of water impact. Part 2. Linearized Wagner problem. *J. Fluid Mech.* **549**, 343–373 (2006).

34. Scolan, Y. M. Hydroelastic behaviour of a conical shell impacting on a quiescent-free surface of an incompressible liquid. *J. Sound Vib.* **277**, 163–203 (2004).

35. Croci, K. *et al.* Mitigation of underwater explosion effects by bubble curtains: experiments and modelling. in *23rd MABS (Military Aspects of Blast and Shock)* 14 (2014).

36. Kowe, R., Hunt, J. C. R., Hunt, A., Couet, B. & Bradbury, L. J. S. The effects of bubbles on the volume fluxes and the pressure gradients in unsteady and non-uniform flow of liquids. *Int. J. Multiph. Flow* **14**, 587–606 (1988).

37. Chuang, S. L. & Milne, D. T. Drop tests of cones to investigate the three-dimensional effects of slamming. in *Report No. 3543, Naval Ship Research and Development Center (Washington D.C.)* (1971).

38. Brennen, C. E. *Cavitation and bubble dynamics*. (Cambridge University Press, 2013). doi:10.1017/CBO9781107338760.

39. Scolan, Y.-M. Hydrodynamic impact of an elliptic paraboloid on cylindrical waves. *J. Fluids Struct.* **48**, 470–486 (2014).

40. Bagnold, R. A. Interim report on wave pressure research. *J. Inst. Civ. Eng.* **12**, 202–226 (1939).

41. Matsumoto, Y., Uda, T. & Takagi, S. The effect of surfactant on rising bubbles. *Fluid Mech. its Appl.* **81**, 311–321 (2006).